Lawrence Berkeley Laboratory
UNIVERSITY OF CALIFORNIA

Materials & Chemical Sciences Division

Reaction Sintering of ZnO-Al_2O_3

W.S. Hong
(M.S. Thesis)

May 1991

Prepared for the U.S. Department of Energy under Contract Number DE-AC03-76SF00098

DISCLAIMER

LBL-30832

REACTION SINTERING OF ZnO-Al_2O_3

Wan-Shick Hong

M.S. Thesis

Department of Materials Science and Mineral Engineering
University of California

and

Materials Sciences Division
Lawrence Berkeley Laboratory
University of California
Berkeley, CA 94720

May 1991

This work was supported by the Director, Office of Energy Research, Office of Basic Energy Sciences, Materials Sciences Division, of the U.S. Department of Energy under Contract No. DE-AC03-76SF00098.

Acknowledgement

I thank God Almighty who guided and enabled me to finish this thesis. Professor Lutgard C. De Jonghe deserves special thanks for his continued encouragement and valuable discussions. I would also like to thank my fellow graduate students, especially Frank Lin, Tim Kueper, and Naomi Naito, for their advices on experimental details and on English writing. I owe a lot to James Wu and John Jacobson in technical matters. Finally, I give thanks to my family in Korea for their love and moral support.

Table of Contents

I. Introduction

The firing processes of ceramic materials are of great importance, since almost all of ceramics are produced by treating at high temperature. During the heat-up, the pore removal is driven by not only the total surface energy reduction, but sometimes also by chemical reaction. Chemical reaction can be expected to influence both the densification kinetics and the microstructural evolution. In addition, because firing at high temperature requires substantial energy consumption, many attempts have been directed to taking advantage of the inherent chemical energy release during reaction sintering to try to obtain better products at lower temperatures.

The term "reaction sintering" stands for the concurrent processes of chemical reaction and densification during the heat-up period.[1)] Usually, the free energy change for the chemical reaction is much larger than that for the reduction in surface area, and therefore the potential advantage of reaction sintering is the high chemical driving force for material transport.[2)] Also, pre-reaction or calcination steps can be eliminated. However, shortcomings of reaction-sintering, such as swelling due to the difference in the diffusivity of each component, lack of homogeneity of the solid state reaction, a change of sample temperature due to the enthalpy variation, and difficulty in controlling the reaction process and microstructure, often outweigh the merits of the reaction sintering. Any expansion of the specimen is usually detrimental to the density of the final product. It has been proposed that for a reaction-sintering system, the compact can densify if

densification precedes the reaction.[3] It was also reported that densification may be possible even in intrinsic swelling systems if other factors work favorably: Particle rearrangement, the involvement of liquid phases, the elimination of surface irregularities, and the formation of sufficient new particle-particle contacts.[4] The relative importance of these events depends on the material, heating rate, atmosphere, particle size, and green density.[5]

So far, studies of the sintering process mostly have not been quantitative because the many variables tend to defeat precise theoretical treatments. Recently, some progress has been made in developing suitable models for microscopic changes and in seeking common rules governing the whole densification behavior. De Jonghe and co-workers developed a loading dilatometry technique which enables the determination of the sintering stress of a densifying powder compact by measuring the macroscopic dimensional changes.[6),7),8] Also, they found that the sintering stress tends to be constant in a wide range of the relative density in many, though not all, systems.[9),10] These observations were made only for a one-component system or a one-component system containing small amounts of additives, dopants or a liquid phase.

The objectives of this study are: First, to study the roles of densification kinetics and reaction kinetics and the relationship of the sintering stress to these kinetics in a two-component system which undergoes both densification and chemical reaction. Second, to evaluate the extent of the densification of this system by investigating the effects of the process variables on the overall sintering behavior.

A model system was chosen following the criteria: a relatively

simple phase relationship, well-studied reaction kinetics, non-hygroscopic, and sinterability in the existing equipment. The ZnO-Al_2O_3 system satisfies all of these conditions and the powders are commercially available. Particle size, heating rate and initial density were chosen as process variables, and all of them were easily adjustable.

II. Background

II-1. Reaction Mechanism of $ZnO-Al_3O_3$

$ZnO-Al_2O_3$ is one of the most frequently used model systems for solid state reaction study, due to its simple phase relationship and well-known reaction kinetics.[11),12)] The exact phase diagram of this system is as yet unknown. What is available is the liquidus line, which is depicted in fig.1.[13)] However, it is well known that the two end members form only one intermediate compound, zinc aluminate spinel. Branson[14)] also showed that the reaction process is not counterdiffusion, but is one-way transfer of ZnO. As temperature increases, zinc oxide diffuses into interstitial positions of aluminum oxide, creating a solid solution. The hexagonal alumina lattice starts to distort due to the strain caused by Zn^{2+} ions. On further reaction, the disordered solid solution changes to the ordered zinc aluminate spinel structure, resulting in the switch of the crystal system from hexagonal to cubic. Molar volumes of $ZnO+Al_2O_3$ and $ZnAl_2O_4$ are 39.47 cm^3 and 40.03cm^3, respectively. Thus, the molar volume increase due to the lattice parameter change is almost negligible.

It is believed that oxygen ions do not diffuse through the spinel layer; only the zinc ions pass through. The zinc ions then recombine with atmospheric oxygen at the spinel-alumina interface to form the spinel phase. Therefore, the reaction should be carried on in air or oxygen. The spinel layer breaks away from the alumina particle, probably owing to thermal expansion mismatch of the two materials, allowing further reaction. The reaction kinetics can be described by

the Carter-Valensi equation which was developed on the diffusion-controlled kinetics model.[15),16)] In this model, a sphere of Al_2O_3 of radius r_o is considered to react over all of its surface with either a finely divided powder or a gas of ZnO.

$$[\ 1 + (Z-1)\alpha\ ]^{2/3} + (Z-1)(1-\alpha)^{2/3} = Z + (1-Z)(kD/r_o^{\ 2})t$$

where Z = the volume of $ZnAl_2O_4$ formed per unit volume of Al_2O_3 consumed

α = fraction of the volume reacted

D = diffusion coefficient

r_o = particle radius

t = reaction time

A plot of the left-hand side of the above equation against time should therefore give a straight line. Branson [14)] calculated the reaction rate constants at various temperatures using this equation, and obtained an Arrhenius plot. The activation energy thus calculated was 54.2 cal/mole.

Leblud *et al.* proposed a model for the expansion of the ZnO-Al_2O_3 system during the reaction.[17)] They found that the reaction and the evolution of the porosity occur in parallel. The porosity of the fired sample increases as a function of the advancement of the reaction. They assumed a simple cubic array of grains with a ZnO/Al_2O_3 radius ratio of $\approx$ 0.8. They hypothesized that the zinc aluminate spinel forms as layers on the alumina spheres. Each point of contact had an angle of aperture of 2θ which was calculated as $\approx 24°$. The geometrical arrangement of their model is depicted in fig.2. This analysis has too many

simplifications about the particle arrangement, particle size distribution, and the actual number of particles in the powder compact. In addition, the sintering temperature they used is only 1000°C, which is too low to cause any meaningful densification. Therefore, their analysis is limited only to the solid state reaction, not covering the "sintering" behavior. However, the hypothesis of the formation of layers of zinc aluminate spinel on the alumina grains within an angle of aperture of 2θ represents a good physical model.

II-2. Sintering Stress

The term "sintering stress" for a densifying powder compact is defined as an equivalent applied stress Σ that would produce the same densification rate for the system at identical geometry, but with surface tension effects absent.[9] In the initial stage sintering, an expression of the sintering stress can be developed using the two-particle model.[18),36)] From the geometry shown in figure 3, assuming an ideal grain boundary control, the diffusive flux occurs in the radial direction, and can be expressed as[19)]

$$j_b = - \frac{D_b \nabla \mu}{kT\Omega} \qquad (1)$$

Where D_b is the grain boundary diffusion coefficient, μ is the chemical potential of the atom, Ω is the volume of an atom, k is Boltzmann constant, and T is the absolute temperature. The total number of atoms crossing along the circumference at the radius per unit time is given by

$$J(r) = - \frac{2\pi r \delta D_b \nabla \mu}{kT\Omega} \qquad (2)$$

where δ is the grain boundary thickness.

Since the displacement rate at the boundary must be independent of r, the rate of approach of the two sphere centers, du/dt, is related to J(r) by:

$$J(r) = \frac{\pi r^2}{\Omega} \frac{du}{dt} \tag{3}$$

From equations (2) and (3),

$$\frac{d\mu}{dr} = -2Ar \tag{4}$$

where A is a constant. Integration of equation (4) gives

$$\mu = -Ar^2 + b \tag{5}$$

Since $\mu = \Omega\sigma_{zz}$, where σ_{zz} is the stress on the boundary, equation (5) can be rewritten as

$$\sigma_{zz} = \frac{B - Ar^2}{\Omega}$$

A and B can be found from the boundary conditions. The first boundary condition is that the stress at the edge of the neck is equal to zero, i.e., $\sigma_{zz}(r=R) = 0$, and the second is that the average stress on the grain boundary,

$$\sigma_{ave} = \int_0^{2\pi} \int_0^{x} \frac{(\sigma_{zz}(r))r \, dr d\theta}{\pi R^2} = \Sigma\phi \tag{6}$$

where Σ is the sintering stress and ϕ is the stress intensification factor, which is defined as the total area divided by grain boundary area. By solving for A and B, the total number of atoms coming out at the edge of the neck per unit time is

$$J(R) = \frac{8\pi D_b \delta \Sigma\phi}{kT} \tag{7}$$

where R is the neck radius. Taking simple cubic Voronoi cells for spherical particles,[36] the total volume transported out of one neck in the time interval Δt is equal to

$$\frac{J(R)\ \Omega\ \Delta t}{2} = \frac{\Delta x\ \pi R^2}{2} \tag{8}$$

where Δx is the change in the corresponding cell center-to-center distance, and the factor of 2 arises because each neck is shared by 2 cells. Assuming isotropy, volumetric shrinkage occurs in all three directions so that

$$\frac{\Delta V}{V} = 3\frac{\Delta x}{x}$$

Therefore, the rate of change in the cell volume is

$$\frac{dV}{dt} = \frac{\Delta V}{\Delta t} = 3\Omega J \frac{x^2}{\pi R^2} \tag{9}$$

The relationship between x and R can be established involving the stress intensification factor, ϕ

$$\phi = \frac{x^2}{\pi R^2} = \alpha \frac{x^2}{R^2}$$

where α is the shape factor which depends on the geometry. Thus, by definition, equation (9) is equal to

$$\frac{dV}{dt} = 3\phi\Omega J$$

The instantaneous volumetric strain rate of the cell is obtained by normalizing dV/dt by the cell volume V, which is equal to x^3.

$$\frac{1}{V}\frac{dV}{dt} = \frac{3\phi\Omega J}{x^3} \qquad (10)$$

The linear densification strain rate, $\dot{\epsilon}_\rho$, is equal to -(1/3V)(dV/dt) so that

$$\dot{\epsilon}_\rho = - \frac{8\pi D_b \delta\Omega\phi^2\Sigma}{kTx^2} \qquad (11)$$

When an external stress is applies, equation (11) may be written in the general form[36]

$$\dot{\epsilon}_\rho = \frac{HD\phi^{(n+1)/2}}{x^n kT} (\Sigma + \sigma_a) \qquad (12)$$

where H is a constant, D is the diffusion coefficient, σ_a is an additional hydrostatic applied stress, n is a constant which depends on the transport mechanism. If we define the densification viscosity, η_ρ, as

$$\eta_\rho = \frac{x^n kT}{HD\phi^{(n+1)/2}}$$

equation (12) can be simplified to[36]

$$\dot{\epsilon}_\rho = \frac{1}{\eta_\rho} (\Sigma + \sigma_a) \qquad (13)$$

A uniaxial applied stress causes a local variation of the chemical potential of the atoms (or vacancies). The atoms migrate from the grain boundaries which are perpendicular to the applied stress direction to those parallel to the applied stress direction.[21] This diffusional creep can be described by a constitutive equation of a similar form to the densification strain rate equation. Starting from equation (1) and considering mass balance, the creep strain rate is expressed as

$$\dot{\epsilon}_c = \frac{H' D\phi^{(n+1)/2}}{kTx^n} \sigma$$

where H′ is a constant and σ is the uniaxilly applied stress which is equal to $3\sigma_a$. More generally

$$\dot{\epsilon}_c = \frac{1}{\eta_c} \sigma = \frac{1}{\eta_c} 3\sigma_a \qquad (14)$$

Then from equations (13) and (14)

$$\dot{\epsilon}_\rho / \dot{\epsilon}_c = (\eta_\rho / \eta_c)(\Sigma/\sigma + 1/3)$$

For balanced densification and coarsening, during which the effect

of the surface redistribution is absent, the ratio, η_ρ/η_c, can be assumed to be constant and equal to 1. Thus the sintering stress, Σ, is directly related to the ratio $\dot{\epsilon}_\rho/\dot{\epsilon}_c$.[6] De Jonghe and co-workers observed that the sintering stress remains fairly constant for a variety of systems.[6),7] The sintering stress may appear to be constant since the most significant factor on which Σ depends is also a part of ϕ. The effect due to the change of ϕ with porosity is compensated by the grain growth.

II-3. Reaction Sintering

Reaction sintering may include oxidation-reduction reactions, the formation of a solid solution or a liquid phase as well as the formation of the intended product.[25] Due to the wide variety of the reaction mechanisms and the strong dependence on various experimental parameters, it is impossible to describe the phenomena occuring during the reaction sintering process on the basis of a complete model. Hence, the studies on reaction sintering have been approached from a practical viewpoint. Also, because of the limited knowledge concerning process control, most of the reaction sintering is being applied to forming compounds for subsequent consolidation. However, the potential exists for direct consolidation of materials into useful engineering shapes by reaction sintering, especially when combined with an external pressure.[26),27] Some well-known reaction sintering systems are Reaction-Bonded-Silicon-Nitride (gas-solid),[28] Si-Al-O-N (liquid-solid),[29] and mullite-zirconia (solid-solid).[30] In all these cases, accomplishment of a homogeneous and complete reaction, high sintered density, and control of the sample dimensions are the major concerns.

Since the completion of the reaction often requires a porous reaction layer to allow a path for further matter transport, and the full densification needs a homogeneous microstructure, precise control of the processing parameters is very critical. Moreover, since the relative importance of each processing variable differs from system to system, knowledge of the reaction mechanism involved is of great importance. If the interaction between densification and reaction does not change the kinetic and thermodynamic factors for each process, in principle, the effect of the processing parameters on the relative rates of the two processes can be addressed.[3)]

Problems arise when the diffusivity of each component in a reaction sintering system differs significantly. The Kirkendall effect then can introduce pore accumulation, and the system swells intrinsically. However, it has been reported from several investigators that even the self-swelling systems can densify under certain conditions.[3),4),32)] The densification may be achieved by increasing the densification driving force, changing the phases of the starting materials, or modifying the microstructure of the green compact. It was proposed by Shen and Brook that the production of dense, fine grained ceramics by reaction sintering was possible if the densification occurs prior to the reaction.[3)] Based on this idea, efforts have been made to bring the densification ahead of the reaction. The kinetics of the two processes may be influenced by particle size, heating rate, sintering temperature, and external pressure.[2)] In general, since densification is driven by surface area reduction whereas reaction is driven by chemical free energy decrease, and since densification can be accelerated by external pressure through equation (12), a smaller

particle size or externally applied pressure increases the ratio of the densification rate to the reaction rate. Depending on the activation energy and material transfer mechanisms of the two kinetics, the sintering temperature and heating rate also increase or decrease the ratio.[31] Young and Wu also reported nearly full densification of the yttrium garnet through reaction sintering by using $YFeO_3$-Fe_2O_3 instead of Y_2O_3-Fe_2O_3.[32] A better densification resulted from microstructure, producing fine grains and voids without trapped pores in the grains.

$ZnAl_2O_4$ is an extreme case of a self-swelling system, because the reaction is controlled by one-way diffusion. The sintering process of this material is not well established due to the lack of engineering applications for the material. Despite the lack of applications, the study of the processing of this material will be beneficial since it may lead to information on the densification of systems which have not yet been successfully densified.

III. Experimental Procedure

III-1. Powder Preparation

Zinc oxide powder (Reagent grade, J.T.Baker Co., purity 99.1%) and aluminum oxide powder (A16SG, Alcoa) were classified by a combined method of sedimentation and centrifuging. To minimize particle size effect, the two particle sizes were made almost the same, and the size distribution was made narrow. The average particle sizes are 0.32 μm and 0.28 μm, respectively, for zinc oxide and alumina. The appropriate amounts were weighed and dispersed in hexane + 0.5 wt% Oloa 1200 solution for better mixing while avoiding agglomeration.[33] The slurry was mixed with a shear mixer at 8000 rpm for 10 minutes and then dried with an infrared lamp. The dried powder mixture was lightly hand-ground using an agar mortar and pestle and was passed through a 150 mesh sieve to break any hard agglomerates.

To see the particle size effect on the densification behavior, powder mixtures of different alumina particle sizes were prepared, while the size of zinc oxide was unchanged. Coarse and medium size (1.5μm and 1μm, respectively) alumina particles were classified from A152SG(Alcoa), and ultrafine(0.06μm) powders were obtained from Baranowsky Co. In this case, the powder was mixed by stirring at 1200 rpm for 1 hour, with a propeller instead of the shear mixer, since the coarse alumina particles acted as abrasives and eroded the mixing blade of the shear mixer.

The pre-reacted zinc aluminate powder was prepared by two methods: coprecipitation and solid-state reaction. For coprecipitation, zinc chloride and aluminum nitrate were weighed to

contain 1:2 molar quantity of Zn^{2+} and Al^{3+} ions and dissolved in distilled water to make 0.2 M aquous solution. While vigorously stirring the solution, an excess amount of NH_4OH was added to form precipitates. The white zinc hydroxide + aluminum hydroxide coprecipitates were filtered and washed with water until they showed no reaction to a 0.125 N silver nitrate solution. The precipitates were dried in a vacuum oven at 100°C for 24 hours and calcined at 1300°C for three hours to form the zinc aluminate phase. For solid-state reaction, an equimolar powder mixture of small particle size zinc oxide and aluminum oxide was prepared and heated at 1300°C for 3 hours in a zirconia crucible. Complete reaction was verified by X-ray diffraction analysis. The reacted powder was ground in the planetary mill for 3 hours using high purity zirconia balls and ethanol. The powder mixture was dried and classified into the desired particle size, and then coated with oloa 1200 as described before.

III-2. Compact Forming and Sintering

The powder was uniaxially pressed into cylindrical compacts of approximately 6mm x 6mm, and then isostatically pressed giving green density of about 64.5 ± 0.5 % of the theoretical density. Samples outside this range were discarded. The coarse particles led to a higher green density when isostatically pressed, thus the compacts containing coarse alumina particles were pressed by the uniaxial press alone. For the powder mixture containing fine-sized alumina powder(0.3μm), powder compacts of two other green densities were prepared by varying the pressing method. One was uniaxially pressed at 0.4ksi followed by cold isostatic pressing at 200ksi, and the other

was uniaxially pressed at 0.5ksi only. The resulting green densities were 69.3 ± 0.3 % and 56.4 ± 0.5, respectively. In all cases, the pressure was allowed to relax slowly for more homogeneous compaction.[34] The pressed pellet was heated to 450°C with a heating rate of 2°C/min from room temperature in order to burn out the binder.

The specimen was sintered in the loading dilatometer up to 1400°C with constant heating rate of 1°C/min, 2°C/min, 4°C/min, and 10°C/min, both with and without the controlled uniaxial load of 0.7N. The sample was cooled rapidly as soon as it reached the sintering temperature. For the heating rate of 10°C/min, the sintering was performed only up to 1250°C due to the limitation of the existing equipment. The initial and final dimensions of the specimen were measured with a micrometer, and the continuous changes of the relative density, strains, and strain rates were calculated. The sintering stress was calculated from the difference of axial strains between the loaded and unloaded sample, assuming that the densification strain for the two cases are the same. In a separate set of experiments, the sintering was terminated at every 100°C interval from 700°C to 1400°C, and the samples were taken out. The dimensions were measured directly and compared with the values obtained from the dilatimeter measurements.

For the reactive sintering experiment, some samples were presintered to the temperature where the reaction was just completed, and fired again from the room temperature to the sintering temperature, in order to see the pure densification behavior.

III-3. Characterization

The samples sintered at selected temperatures were cut with a diamond saw, being aligned with the cross section parallel to the load-applying direction. The sectioned specimens were mounted with epoxy resin, polished with SiC paper and diamond paste, and then thermally etched at temperatures 200°C below the sintering temperature for 2 hours. The polished and etched surfaces were gold-coated and observed by scanning electron microscpy.

Phase compositions and the amount of zinc aluminate formed were determined by an X-ray powder diffractometer.

IV. Results and Discussion

IV-1. Powder preparation

The X-ray diffraction patterns of the zinc aluminate powder prepared by coprecipitation and solid-state reaction are shown in fig.4. The figure shows that the solid state reaction method converts all the zinc oxide and aluminum oxide into zinc aluminate whereas the coprecipitation methods retains an appreciable amount of unreacted alumina. This unreacted alumina phase may be due to the lower solubility of the aluminum hydroxide in the common solution than of zinc hydroxide. The quantification of the precipitated amount of Zn^{2+} and Al^{3+} ions was attempted, but it could not easily be controlled in the experiment. Since the other characteristics of the coprecipitated powder, such as average particle size and particle size distribution, were not so much better than those of the conventionally calcined powder, the coprecipitation method was discarded.

The classification of the alumina powder was successfully achieved by a combined method of centrifuging and sedimentation, using H_2O as the dispersing medium. Since the classification data were difficult to reproduce, the average particle size differed slightly from batch to batch. Thus all the batches were collected and classified several more times.

Zinc oxide showed a high agglomeration tendency and could not be classified very well. Also, the commercial zinc oxide powder contains large amounts of plate-like particles which have larger specific surface area than spherical or equiaxed particles. To obtain a better result,

the dispersing medium was switched to ethanol, which is a less polar liquid, and the powder slurry was agitated ultrasonically even longer. In spite of this, the resultant particle size distribution was still broader than that of alumina, and could not be made any narrower.

IV-2. Sintering Behavior of the Powder Compacts

Fig. 5 shows the relative densities of the three specimens plotted against the temperature. The calcined sample started to shrink at around 1000°C and showed the familiar sigmoidal curve. The measured strain agreed well with the value calculated from the loading dilatometer data within ~2% error. The shrinkage occured uniformly in both the axial and the radial direction, and the overall sintering behavior was in good agreement with previous work on ZnO, Al_2O_3, etc.[7] When the uniaxial load of 0.7N was applied, the ϵ_r vs. ϵ_z plot showed a linear curve with slope ≈0.6 as shown in fig.6(a).

The reaction sintered sample started to expand above 700°C, remained unchanged between 1050°C-1150°C, and then began to shrink. As described elsewhere, the spinel formation reaction between ZnO and Al_2O_3 is accompanied by lattice expansion. Because the theoretical density difference between $ZnAl_2O_4$ and ZnO-Al_2O_3 (4.58 g/cm^3 and 4.65 g/cm^3, respectively) is small, indicating that the molar volumes of the two are almost the same, the expansion is due to the production of Kirkendall porosity rather than to the intrinsic density difference. The phases existing in the reaction sintered compact at several temperatures were verified by X-ray powder difractometer and the results are depicted in fig.7. Until 800°C, only the peaks of ZnO and Al_2O_3 can be seen. However, the diffractogram at 900°C indicates the significant formation

of $ZnAl_2O_4$. The conversion of ZnO and Al_2O_3 into $ZnAl_2O_4$ is shown to be completed at 1000°C, where the expansion nearly stopped. Therefore, the reaction and expansion are thought to go in parallel.

The sample under no load deformed isotropically until the end of the heating, and the measured dimensions matched well with the values calculated within an experimental error. However, for the loaded sample, the ratio of ϵ_r/ϵ_z was no longer constant throughout the heating period.

During the initial stage, since the expansion force due to chemical reaction was large enough to overcome the applied load (0.7N), the sample expanded isotropically in spite of the load, i.e., no creep occured during the chemical reaction except for a short period at the end of the reaction. The measured sample dimension and density were the same as those of the unloaded sample during this expansion period. After showing no subsequent densification between 1050°C-1150°C, the sample began to densify and the creep occured at the same time. The axial and radial strains of the reaction-sintered sample were plotted in fig.6(b). The ratio of ϵ_r/ϵ_z after 1100°C is shown to be irregular because it was calculated from the dimensions of the green compact. To deal with this problem, specimens were presintered at 1050°C, taken out, measured, and fired again up to 1400°C under the load. The presintering procedure did not affect the final sample dimension, and the sintering behavior after the reaction(above 1050°C) turned out to be similar to that of $ZnAl_2O_4$ compact. The ratio of ϵ_r/ϵ_z was constant during the reaction period, showing a value of ≈ 1, but dropped to ≈ 0.6 when shrinkage started, and then remained at this value for the rest of the firing period.

The other calcined samples were prepared to have the same density as that of the presintered specimen, i.e., the density at the point where the reaction was just completed, so that the pure densification behavior of the reaction sintered compact can be compared. The relative density curve of fig.5 shows that the densification starting point of the calcined sample just crosses the expansion end point. Therefore, it can be concluded that the chemical reaction and the densification occur separately and independently in the ZnO-Al_2O_3 system, under the condition of same Al_2O_3 and ZnO particle sizes and a constant heating rate of 4°C/min. In this case, the reaction and the densification are two consecutive steps without overlap. The supporting facts for this conclusion are; i)Material transfer occurs in an opposite direction to densification during the reaction.(reaction caused expansion) ii)The expansion of the compact at the first stage was not affected by the applied load. If the reaction had involved any densification, the sample dimension during this period would have been affected by the applied load. iii)The shrinkage started above 1150°C, whereas the reaction was completed before 1050°C, and therefore there was an 100°C temperature gap between reaction completion and densification initiation. iv)The shrinkage of the calcined sample upto 1100°C was small enough to be neglected, implying that the densifying transport mechanisms were not activated during the reaction. iv)The SEM pictures showed no appreciable neck formation until 1100°C. Thus, it can be thought that the reaction/expansion and the densification do not overlap, and that they can be analyzed separately.

Fig.8 illustrates the temperature derivative of densification

strain, $(1/\rho)(d\rho/dT)$, of the three samples. The valley of the $(1/\rho)(d\rho/dT)$ curve of the reaction sintered sample corresponds to the expansion. The peaks of the two calcined specimens occur at nearly the same temperature. However, the maximum of the lower green density specimen is higher. This behavior was discussed in Rahaman *et al.*'s work.[35] The height of the reaction sintered peak appears to be much smaller than the others and was shifted toward the high temperature region, indicating much less densification.

The ratio of densification strain rate over creep strain rate, $\dot{\epsilon}_\rho/\dot{\epsilon}_c$, was calculated from the creep data and plotted in fig.9. The ratio $\dot{\epsilon}_\rho/\dot{\epsilon}_c$, the quantity that can be related to the sintering stress, increased as the temperature went up, and then exponentially decreased. The curve up to 1000°C is not so meaningful because both the densification and the creep up to this temperature are negligible. Even a tiny error in the calculation of either densification strain rate or creep strain rate may produce a large fluctuation of the ratio between the two in this temperature range. In fig.9(a), the curves of the two calcined samples appear to be almost identical, when plotted against temperature, except for a slightly earlier maximum of the lower green density sample. This result seems to contradict Rahaman *et al.*'s conclusion that the ratio of $\dot{\epsilon}_\rho/\dot{\epsilon}_c$ increases according to the green density.[37] However, no conclusion can be drawn from the current result because only two curves are not sufficient to be discussed systematically.

The variation of the sintering stress can be seen more clearly when plotted against the relative density.(fig.9(b)) The sintering pressure increased suddenly when the denfication started and then tailed

off exponentially. This phenomenon is thought to be due to the increase of the nondensifying transport mechanisms which contribute to the particle coarsening. SEM micrographs of the calcined powder compact of initial density of ≈64% are shown in fig.10. Noticeable neck formation occured around 1100°C (See fig.10(b)) where the sintering stress curve rapidly rises, and significant coarsening occured above 1200°C (fig.10(c)) where the curve began to fall. This relationship between the sintering stress and the microstructure evolution is consistent with the previous analysis by Ghirlanda and De Jonghe.[22)]

IV-3. Sintering Stress in Reaction Sintering

During the reaction period, the ratio $\dot{\epsilon}_\rho/\dot{\epsilon}_c$ could not be calculated except for a short period at the end of the reaction, since no detectable creep occured. Also, since the driving force of the material transport is almost purely chemical during this period, the ratio $\dot{\epsilon}_\rho/\dot{\epsilon}_c$ cannot be related to the sintering stress, although it could be calculated. However, at the end of the reaction, the driving force for reaction becomes very small and the expansion is only slightly affected by the applied load. Thus the $\dot{\epsilon}_\rho/\dot{\epsilon}_c$ ratio showed a negative value as shown in fig.9, conforming to the physical meaning of a negative sintering stress for the expanding compact. This value abruptly increased and then also tailed off, but not as much as in the calcined sample. The peak of the $\dot{\epsilon}_\rho/\dot{\epsilon}_c$ curve of the reaction sintered sample is also smaller than those of the calcined specimens, implying a weaker driving force for sintering. These discrepancies from the calcined counterparts can also be explained by taking the microstructure into account.

The SEM micrographs of fig. 11 show the microstructural evolution of the reaction sintered compact. At 900°C (fig.11(a)), grains are in intimate contact with each other, inidicating the swelling of alumina grains by "absorbing" zinc oxide. As the reaction proceeds further, the porosity increases. Microstructures at 1000°C (fig.11(b)), and 1100°C (fig.11(c)) show little difference, agreeing well with the plateau of the densification curve in fig.5. As the temperature increases, the particles coarsen and the pores are filled. From fig.10 and 11, the grain growth in the reaction sintered sample is comparable to that in the calcined sample. Yet, it can be noticed that the porous 3-dimensional particle network is formed by the solid state reaction, and developed as the sintering proceeded.(fig.11 (d)-(f)) This 3-D skeleton does not collapse easily, but thickens as the temperature is raised, showing a smaller apparent sintering stress(fig.9). This sintering stress does not appear to decrease very much because of a decrease in the creep rate. Photos of the loaded specimens were taken with the specimen aligned with the load-applying direction, and, for simplicity, only the one taken at 1400°C was displayed in fig.12 along with its unloaded counterpart. Comparison of the microstructures of unloaded (fig.12(a)) and loaded compacts (fig.12(b)) does not show much difference.

This result means that this porous structure of the reaction-sintered sample not only resists densification but also resists the diffusional creep. As a result, the creep strain rate becomes smaller and the ratio of $\dot{\epsilon}_\rho/\dot{\epsilon}_c$ becomes larger, preventing the sintering stress from dropping quickly. This may also be understood through Chu's analysis of the pre-coarsening procedure in the sintering of ZnO.[36]

The pre-coarsening of the particles in the powder compact at a lower temperature yielded a more uniform particle size distribution, which in turn stabilized the microstructure. In the reaction sintering system of ZnO-Al_2O_3, Al_2O_3 particles "grow" as they react with ZnO. Smaller Al_2O_3 particles grow faster than larger particles because they are more reactive, resulting in a more homogeneous size distribution. This system could have had a bigger driving force for sintering, but the highly porous particle network prevents the compact from further densification. Yet, the more uniform size distribution may help the sintering stress from decreasing rapidly.

It must also be noted that all three curves in fig. 9(b) converge exponentially to the value of ≈ 2. The extention of the tail of the reaction sintered specimen overlaps with the other two curves. This means that the sintering stress of this system tends toward a constant value, indicating the stabilization of the microstructure. The average particle size of the reaction sintered specimen at its densification starting point (fig.12(c)) is smaller than that of the calcined sample. (fig.11(a)) Without other factors, the sintering stress of the former might be bigger than that of the latter. However, the particles in the reaction sintering system coarsened faster, causing the two grain sizes at 1400°C to not differ that much. This behavior means that the microstructure evolves toward a common trend, and this effect may cause a tendency for a powder compact to have a fixed sintering stress at a certain density. This explanation can be only applicable when the system has enough surface energy to sinter.

So far, it is observed in this reaction sintering system that there is no overlap of reaction and densification and that the

microstructural change due to the chemical reaction reduces the sintering stress significantly. However, as discussed in Chapter II, densification of the self-swelling system may be possible if the densification precedes the reaction.[3] This can be achieved by either delaying the reaction or bringing the densification forward. The reaction may be delayed when a high heating rate, loose powder compaction or larger particles is used. These experimental parameters, however, may retard the densification as well. In other words, it is worth considering the modification of the microstructure of the starting sample to prevent the formation of the porous particle network. The effects of these variables will be discussed in the following sections.

IV-4. Effect of Heating Rate

Fig. 13(a) and 13(b) illustrate the evolution of the relative density of the calcined, and reaction sintered samples, respectively, at various heating rates. It is seen that the heating rate does not affect the final density very much. In all cases, both the density and the $(1/\rho)(d\rho/dT)$ curves are shifted to higher temperatures as the heating rate increases.(fig.14) This trend is more obvious during reaction than during the densification. Although a higher heating rate delayed the reaction appreciably, it does not seem to make the reaction overlap with densification. In the $(1/\rho)(d\rho/dT)$ vs. density plot in fig.15(b), it is seen that all curves are identical within experimental error. This result means that the increase of the heating rate does not help achieve a higher density. This conclusion may be weak, for the employed heating rates do not have a wide span. However, since a higher heating rate neither reduces the extent of the expansion nor increases that of the

shrinkage, it seems not to have a strong effect on obtaining a denser material. The $\dot{\varepsilon}_\rho/\dot{\varepsilon}_c$ plot in fig.16(b) and fig.17(b) also shows that the sintering stress at a density was not affected by the heating rate.

The densification strain rate (time derivative of the densification strain) can be calculated simply by mutiplying the heating rate by $(1/\rho)(d\rho/dT)$. As the heights of all peaks of $(1/\rho)(d\rho/dT)$ curves in fig.14 are nearly the same, it can be easily shown that the magnitude of the densification rate is proportional to the heating rate. Similar results have been reported in several papers, and a theoretical explanation was proposed in De Jonghe *et al.*'s analysis about the proportionality of the densification rate to the heating rate in a system undergoing significant coarsening.[31] In Rahaman and De Jonghe's analysis of $ZnFe_2O_4$ system, it was reported that the peak of the $(1/\rho)(d\rho/dT)$ curve was shifted toward the lower temperature region as the heating rate increased.[2] They attributed this behavior to the interplay between the reaction and the densification. In the ZnO-Al_2O_3 system, which has no overlap of the reaction and the densification, such a behavior was not observed. This result supports Rahaman's idea that the deviation from this tendency may be due to the interplay between the reaction and the densification.

IV-5. Effect of Green Density

Fig. 18 shows the relative density change of powder compacts having different green densites. The specimen with a higher green density expanded more and densified less than those of lower green densites, although the final density is higher. The volume increase after reaction, $\Delta\rho = \rho_{reac} - \rho_{init}$, becomes larger as the green density

is higher. As seen in the fig.19, the depth and width of the valley of the temperature derivative of the densification strain curve was affected minimally by changes in the green density.

However, the ratios of the initial density over the density after reaction, ρ_{reac}/ρ_{init} of the three specimens are the same for all green densities

$$\frac{\rho_{reac}}{\rho_{init}} = \frac{69.33}{56.21} = \frac{64.65}{52.34} = \frac{56.33}{45.35} = 1.24$$

It implies that the extent of expansion is related to the change of the distance between particle centers in the green compact.

In the densification region, the height of the peak of $(1/\rho)(d\rho/dT)$ curve becomes larger as the green density is increased, and all peaks are located at the same temperature.(fig.19(a)) This result is consistent with that of the calcined samples shown in fig.8., and also with those reported in another paper by Rahaman *et al.*[37] Thus, the densification enhancement effect of initial compaction becomes less likely as the green density is increased.

Fig.20 depicts the ratio of $\dot{\epsilon}_\rho/\dot{\epsilon}_c$ of the three specimens. The plot against the temperature seems to lack a pattern. However, in the plot of $\dot{\epsilon}_\rho/\dot{\epsilon}_c$ vs. relative density, it must be noticed that the upper parts of the three curves fall on a common line. This implies that the sintering stress at these densities is the same regardless of the green density. Taking into account the calcined sample, this implication is quite reasonable, because all the sintering stress curve of this system converge to the value of ≈2. At the onset of the densification, the data deviate from this trend, especially by showing larger values,

because of the extremely small creep strain rate. As mentioned earlier, even a slight numerical error causes large data scattering in the very early stage of sintering.

IV-6. Effect of Particle Size

The relative density change of the powder compacts containing various sizes of alumina particles is plotted in fig.21. It can be seen that the particle size has the most significant effect on the overall sintering behavior of this system. The average sizes of the coarse, medium, fine, and very fine alumina particles are 1.5μm, 1μm, 0.3μm, and 0.06μm, respectively. The compact of the coarse alumina particle expanded, that of the medium particles shrank slightly following expansion, and the fine particle compact densified to some extent following expansion. The coarser particles certainly retarded the reaction, but lead to larger expansion and less shrinkage.

A drastic change occured when the very fine alumina powder was employed. The green compact could not be made as dense as the others, and yet the final density became much higher than any other samples. Moreover, the compact underwent almost no expansion. This result may be due to the large specific surface area, which advances the densification kinetics toward a lower temperature region, and a particle arrangement in the compact which is more advantageous to shrinkage. The $(1/\rho)(d\rho/dT)$ curve in fig.22 illustrates an outstanding peak of the very fine sized compact, which is located well ahead of the others. Also, the $\dot{\epsilon}_\rho/\dot{\epsilon}_c$ curve in fig. 23 shows that both the reaction and the densification occured at lower temperatures, and that the expansion was soon overwhelmed by the shrinkage.

IV-7. Factors Affecting Expansion and Shrinkage

A theoretical model of the expansion in the ZnO-Al_2O_3 system was proposed by Leblud *et al.*[17] They assumed a simple cubic array of Al_2O_3 and ZnO grains, similar to the NaCl structure(fig.2). Layers of zinc aluminate were thought to be formed on the alumina grains within an angle of aperture of 2θ. The Al_2O_3 grains grew by converting to $ZnAl_2O_4$ and ZnO grains disappeared. The cell parameter was expressed as $R_{A,t}$+ $R_{Z,t}$+ r_t, where $R_{A,t}$, $R_{Z,t}$ and r_t are the radius of alumina sphere, the radius of zinc oxide sphere and the thickness of the zinc aluminate layer, respectively. Although the physical meaning of the aperture angle and the relationship between the reaction advancement and porosity are quite reasonable, there are questions which arise about some of the points. First, the simple cubic array becomes an fcc array of $ZnAl_2O_4$ grains when the reaction is completed, if the relative positions of the alumina particles do not change. Since the fcc array has a higher packing efficiency, the final density should be higher. Second, after some time t, the alumina grains with zinc aluminate layer in the diagonal direction touch each other, and the reduction in the radius of zinc aluminate may not contribute to the change in the cell parameter.

In the real system, the alumina grains are in contact not only with zinc oxide grains but also with other alumina grains. As the reaction proceeds, the alumina particles grow with the formation of the zinc aluminate layer and their center-to-center spacing increases. There is also a possibility that, once the alumina particles touch each other, the growth in their center-to-center direction may be hindered and the growth in other directions may be enhanced. If this happened,

the expansion would stop at the early stage of reaction and would be suppressed by an externally applied load. However, this phenomenon was not observed. The compacts expanded uniformly regardless of the applied load, and the whole dimensional change was unaffected by the load, indicating a very large driving force for expansion.(Section IV-2) The volume change of an individual alumina grain according to the reaction is

$$\frac{(\text{molecular weight} / \text{theoretical density}) \text{ of } ZnAl_2O_4}{(\text{molecular weight} / \text{theoretical density}) \text{ of } Al_2O_3} = 1.557$$

Hence, if the alumina particles are all connected with one another, the volume of the powder compact will also change by a factor of 1.557. However, this volume increase is partially compensated by the consumption of the zinc oxide grains.

This consideration may explain why the compacts having different green density expanded by the same factor, 1.24, in section IV-4. If the alumina grains are not initially touching as in fig.2, the mean spacing between the particles may be related to the green density, and a compact of higher green density will expand earlier and further than one of lower green density. However, all compacts expanded at the same time and to the same extent. Thus, it can be concluded that a denser compaction only increases the coordination number of each particle, i.e., the local packing efficiency, and the extent of expansion is only governed by the pushing-apart of the alumina grains. Another explanation is to consider the pores surrounded by particles as building units of the compact. That is, in an actual green compact, particles form rings or shells, producing large pores. Sizes of these rings and

shells decrease as the green density increases, but each ring or shell will expand along with the reaction, by the same factor regardless of its size. In turn, the extent of the overall volume change is the same for all green densities.

This analysis is consistent with the observation that the higher heating rate did not help prevent the compact from swelling. A higher heating rate or larger particle size does retard the reaction, but each of them also retards the densification. Even if the reaction occurs after the densification, it can be proposed from microstructural consideration that the compact may not densify under certain conditions. The advancement of the densification ahead of the reaction can be one condition for the production of a denser material, but by itself is not sufficient. Suppose that the compact fully densified before any reaction. Fig. 24(a) shows schematically the densification of alumina and (b) the densification of zinc oxide. As seen in this diagram, although full density can be achieved before the reaction, the Kirkendall effect introduces porosity and the compact swells as the alumina grows at the expense of zinc oxide. Hence, in addition to the requirement that densification occurs first, balanced diffusivities of the two components are also required to obtain a higher density in reaction sintering.

Reducing the alumina particle size turned out to be successful in accomplishing appreciable densification. In addition to a larger specific suface area, the small particle size has the added advantage of allowing modification of the packing arrangement. Therefore, the Al_2O_3/ZnO particle size ratio, R_A/R_Z, is thought to be more important to obtain a better densification. Alumina particles much smaller than the

zinc oxide can easily be accomodated in the voids in ZnO packing. Consider the simplified diagrams in fig.25. It can easily be seen that, when the alumina grain is bigger than or equal to the zinc oxide, the disappearance of zinc oxide cannot make enough room for alumina growth. In contrast, when the alumina grains are sufficiently small compared to the zinc oxide, they can occupy the voids formed by the ZnO consumption, accomodating the strain due to the expansion. This explanation was verified by microstructure examination. Fig.26 shows actual microstructures of the powder compacts having various R_A/R_Z ratios. All three compacts were sintered up to 1400°C with a heating rate of 4°C/min. When the alumina grains are larger than or equal to the zinc oxide grains(fig.26(a) and (b)), the resulting microstructure is a loosely packed zinc aluminate particles with large voids in the ZnO sites. When the alumina grains are smaller than zinc oxide grains(fig.26(c)), spaces in the zinc oxide sites are filled with the $ZnAl_2O_4$ particles through particle rearrangement.

It is also noted that the average grain size of very fine sized compacts(fig.26(c)) is comparable to that of fine sized compacts. (fig.26(b)) This significant grain growth is believed to be responsible for the decrease in the $\dot{\epsilon}_\rho/\dot{\epsilon}_c$ ratio in fig.22. In spite of this substantial grain growth, the final density is higher, which may be due to particle rearrangement during the reaction. Therefore, it can be concluded that particle arrangement in the initial packing has a strong influence on the densification of this reaction-sintering system. The initial packing arrangement, which leads to more particle-particle contacts and less voids after the reaction, is important for densification in this system. For a favorable powder packing, efforts

must be directed either to accomodate the intrinsic expansion by void spaces or to compensate the growth of the reaction layer by the consumption of the reacting components. Further investigation for varios particle sizes is reqired for a more specific conclusion.

In addition to reducing the R_A/R_Z ratio, coating the alumina particles with an equimolar amount of zinc oxide might be a way to improve the particle arrangement. Since the difference between the molar volumes of $ZnAl_2O_4$ and a ZnO-Al_2O_3 mixture is negligible as mentioned in section IV-2, net dimension of each coated powder will not change much after the reaction, if a smooth and complete coating can be done. Such a powder compact is expected to undergo little expansion during the reaction, and to densify better than an uncoated powder mixture, unless the coating phase sinters to form a rigid network before the reaction is completed. Experimental confirmation of this idea is strongly demanded.

Fig.26(a) also reveals an internal sub-structure which is similar to that observed by other workers in the reaction sintering system of Al_2O_3-TiO_2.[38),39),40)] In this picture, it can be clearly seen that each particle consists of tiny sub-grains. In the Al_2O_3-TiO_2 system, such a structure was explained either in terms of fine aluminum titanate grains arranged in highly oriented domains which were surrounded by cracks[39),40)] or in terms of a relic structure representative of the oxide matrix prior to reaction.[38)] The latter explanation sounds more likely because the sub-grain boundaries do not look like microcracks. Each sub-grain which made up the starting alumina particle is thought to retain its own orientation after the reaction, and the sub-grain boundaries appear more obviously due to the difference in expansion

between the sub-grain matrix region and the sub-grain boundary region. As the alumina particles become smaller(fig.26(b) and (c)), this sub-structure appears less likely.

From the observation of the density variation and microstructure in the ZnO-Al_2O_3 reaction sintering, it is inferred that the near-net shape forming of a honeycomb structure may be possible by adjusting the particle size and the sintering temperature.

V. Summary

The sintering behavior of the reaction sintering system of ZnO-Al_2O_3 was studied. The reaction sintered sample expanded during the reaction, and then started to densify. With a heating rate of 4°C/min and an average particle size of ≈0.3μm, chemical reaction and densification seemed to occur separately, as the densification kinetics were overwhelmed by the reaction kinetics. The expansion due to the chemical reaction was not affected by an applied stress of 0.24MPa, whereas diffusional creep occurred after the reaction, changing the ratio of radial to axial strain. Hence, the loading dilatometry technique, which is based on the assumption of constant ϵ_r/ϵ_z ratio, had to be modified. The chemical reaction changed the microstructure significantly, reducing the sintering driving force. However, as the densification proceeded, the sintering stress did not decrease as much as in the calcined sample, probably benefiting from the lower creep rate and more stabilized microstructure relative to that in the calcined sample. Also, the sintering pressure converges to a specific value, implying a tendency of the microstructure to stabilize.

Heating rate and green density were shown to have little effect on the extent of shrinkage, while alumina particle size affected the whole sintering behavior drastically. A higher heating rate and larger particle size retarded the reaction appreciably, but samples fail to achieve a larger final density. Neither the densification kinetics nor the reaction kinetics were sensitive to the green density, except for a little enhancement of the densification rate by looser compaction.

Reducing the alumina particle size was most beneficial in obtaining a denser product because of the large driving force for sintering and accomodation of the volume expansion by the large voids which were formed in the powder compact when ZnO particles were consumed.

It can be concluded that the particle arrangement in the initial packing has a strong effect on the densification of $ZnO\text{-}Al_2O_3$ reaction-sintering system. Control of the initial packing by changing the R_A/R_Z ratio was attempted, and was shown to produce a better densification. Densification in the reaction sintering may not be accomplished simply by retarding the reaction, but possibly by increasing the surface energy and modifying the particle arrangement.

VI. References

1) D.Kolar, *Sci. Ceram.*, 11 199 (1981)

2) M.N.Rahaman and L.C.De Jonghe, *"Reaction Sintering of Zinc Ferrite: Effect of Heating Rate"*, LBL Report DE-AC03-76SF00098 (1990)

3) Y.Shen and R.J.Brook, *Sci. Sintering*, 17 35 (1985)

4) R.M.German, A.Bose, and N.S.Stoloff, *"Powder Processing of High Temperature Aluminides"*, in *High Temperature Ordered Intermetallic Alloy 3*, p.403-414, Ed. by C.T.Lin, A.I.Taub, N.S.Stoloff, and C.C.Koch, Materials Research Society, Pittsburgh (1989)

5) R.M.German, *Liquid Phase Sintering*, p.65-99, Plenum Press, New York (1985)

6) M.N.Rahaman and L.C.De Jonghe, *J. of Mater. Sci.*, 22 4326 (1987)

7) M.Y.Chu and L.C.De Jonghe, *Acta Metall.*, 37 [5] 1415 (1989)

8) L.C.De Jonghe and M.N.Rahaman, *Rev. Sci. Instrum.*, 55 [12] 2007 (1984)

9) L.C.De Jonghe and M.N.Rahaman, *Acta Metall.*, 36 [1] 223 (1988)

10) M.N.Rahaman and L.C.De Jonghe, *J. Am. Ceram. Soc.*, 73 [3] 602 (1990)

11) W.D.Kingery, H.K.Bowen, and D.R.Uhlmann, *Introduction to Ceramics*, p.420-425, 2nd Ed., John Wiley & Sons, New York (1972)

12) H.Schmalzried, *Solid State Reactions*, Academic Press, New York (1974)

13) E.N.Bunting, *Bur Standards J. research*, 8 [2] 280 (1932)

14) D.L.Branson, *J. Am. Ceram. Soc.*, 48 591 (1965)

15) R.E.Carter, *J. Chem. Phys.*, 34 2010 (1961)

16) R.E.Carter, *J. Chem. Phys.*, 35 1137 (1961)

17) C.Leblud, M.R.Anseau, E.Di Rupo, F.Cambier, and P.Fierens, *J. Mater. Sci.*, 16 539 (1981)

18) R.M.Cannon, *unpublished manuscript* (1990)

19) D.L.Johnson, *J. Appl. Phys.*, 40 192 (1969)

20) M.N.Rahaman, L.C.De Jonghe, and R.J.Brook, *J. Am. Ceram. Soc.*, 69 53 (1986)

21) C.Herring, *J. Appl. Phys.*, 21 437 (1950)

22) M.Ghirlanda, M.S. Thesis, University of California, Berkeley (1990)

23) F.B.Swinkels and M.F.Ashby, *"Role of Surface Redistribution in Sintering by Grain Boundary Transport"*, in *Powder Metallurgy*. p.1 (1980)

24) C.Herring, *J. Appl. Phys.*, 21 301 (1950)

25) F.J.C.M.Toolenaar and M.T.J.Verhees, *J. Mater. Sci.*, 23 856 (1988)

26) Y.Miyamoto, M.Koizumi, and O.Yamada, *J. Am. Ceram. Soc.*, 67 C224 (1984)

27) O.Yamada, Y.Miyamoto, and M.Koizumi, *Ceramic Bull.*, 64 319 (1985)

28) G.Braun *et al.*, *J. Thermal Anal.*, 33 [2] 479 (1988)

29) M.Mitomo, N.Kuramoto, and Y.Inomata, *J. Mater. Sci.*, 14 2309 (1979)

30) A.Leriche, F.Cambier, and R.J.Brook, *"Study of some Factors Influencing the Microstructure Development of Mullite-Zirconia Composites Obtained by Reaction Sintering"* in *Complex Microstructure*, p.167-177, Ed. by R.Stevens and D.Taylor, Brit. Ceram. Soc., No.42 (1989)

31) L.C.De Jonghe, M.N.Rahaman, and M.Y.Chu, *"Effect of Heating Rate on Sintering and Coarsening"*, *J. Am. Ceram. Soc.*, to be published

32) R.J.Young, T.B.Wu and I.N.Lin, *Mat. Res. Bull.*, 22 1475 (1987)

33) M.W.Weiser, Ph.D. Thesis, University of California, Berkeley (1987)

34) N.Naito, L.C.De Jonghe, and M.N.Rahaman, *J. Mater. Sci.*, 25 1686 (1990)

35) M.N.Rahaman and L.C.De Jonghe, *"Sintering of Ceramic Particulate Composites: Effect of Matrix Density"*, *J. Am. Ceram. Soc.*, to be published

36) M.Y.Chu, Ph.D. Thesis, University of California, Berkeley (1990)

37) M.N.Rahaman, L.C.De Jonghe, and M.Y.Chu, *"Effect of Green Density of Densification and Creep During Sintering"*, *J. Am. Ceram. Soc.*, to be published

38) H.A.J.Thomas and R.Stevens, *"Microstructure Development during the Reaction Sintering of Alumina and Titania to Produce Aluminum Titanate"* in *Complex Microstructures*, p.117-122, Ed. by R.Stevens and D.Taylor, Brit. Ceram. Soc., No.42 (1989)

39) K.Hamano, Y.Ohya, and Z.Nakagawa, *J. Ceram. Soc. Japan*, 91 [2] 94 (1983)

40) Y.Ohya, M.Hasegawa, Z.Nakagawa and K.Hamano, *Report of the Research Laboratory of Engineering Materials*, Tokyo Institute of Technology, No.12, 81 (1987)

Figure Captions

Figure 1. Phase diagram of ZnO-Al_2O_3 system

Figure 2. Geometrical arrangement showing the formation of layers of zinc aluminate spinel on the alumina grains within and angle of aperture of 2θ.[17)]

Figure 3. Geometry of neck region in the two particle sintering model[18)]

Figure 4. XRD pattern for powders obtained by coprecipitation and by solid-state reaction, A:alumina, Z:zinc oxide, ZA:zinc aluminate spinel, (a)coprecipitaion (b)solid-state reaction

Figure 5. Relative density change of calcined, and reaction sintered specimens according to temperature

Figure 6. Radial strain vs. axial strain of (a)calcined sample (b)reaction sintered sample

Figure 7. X-ray diffractograms of reaction sintered compacts heated up to (a)800°C (b)900°C (c)1000°C

Figure 8. Temperature derivative of densification strain plotted against (a)temperature (b)relative compact density

Figure 9. Ratio of densification strain rate over creep strain rate, $\dot{\epsilon}_\rho/\dot{\epsilon}_c$, versus (a)temperature (b)relative density

Figure 10. Scanning electron micrographs of polished surfaces of calcined samples sintered at (a)1000°C (b)1100°C (c)1200°C (d)1300°C (e)1400°C

Figure 11. SEM pictures of polished sections of reaction sintered specimens, (a)900°C (b)1000°C (c)1100°C (d)1200°C (e)1300°C (f)1400°C

Figure 12. Scanning electron micrographs of reaction-sintered samples at 1400°C, (a)unloaded (b)loaded. Load was applied in vertical direction

Figure 13. Relative density change at various heating rates, (a)calcined (b)reaction sintered compact

Figure 14. $(1/\rho)(d\rho/dT)$ vs. temperature at various heating rates, (a)calcined (b)reaction sintered specimen

Figure 15. $(1/\rho)(d\rho/dT)$ vs. relative density at various heating rates, (a)calcined (b)reaction sintered

Figure 16. Ratio of $\dot{\epsilon}_\rho/\dot{\epsilon}_c$ vs. temperature at different heating rates, (a)calcined (b)reaction sintered

Figure 17. $\dot{\epsilon}_\rho/\dot{\epsilon}_c$ vs. relative density at different heating rates, (a)calcined (b)reaction sintered

Figure 18. Density change of the reaction-sintered powder compacts of various green densities,

Figure 19. $(1/\rho)(d\rho/dT)$ for various green density vs. (a)temperature (b)relative density

Figure 20. $(\dot{\epsilon}_\rho/\dot{\epsilon}_c)$ for differnt green density vs. (a)temperature (b)relative density

Figure 21. Effect of alumina particle size on density.

Figure 22. Effect of alumina particle size on the temperature derivative of densification strain plotted against (a)temperature (b)relative density

Figure 23. Effect of alumina particle size on the ratio of $\dot{\epsilon}_\rho/\dot{\epsilon}_c$ vs. (a)temperature (b)relative density

Figure 24. Hypothetical schemes of the expansion of pre-densified ZnO-Al_2O_3 composite, Unshaded area: Al_2O_3, Shaded with lines:

ZnO, Shaded with dots: $ZnAl_2O_4$, (a)when ZnO densified first (b)when Al_2O_3 densified first

Figure 25. Schematic diagrams of the expansion ZnO-Al_2O_3 reaction system for different alumina / zinc oxide particle size ratio R_A/R_Z, (a)$R_A/R_Z > 1$ (b)$R_A/R_Z \approx 1$ (c)$R_A/R_Z \ll 1$

Figure 26. SEM micrographs of sintered microstuctures resulting from various R_A/R_Z ratios in the green compacts, (a)$R_A/R_Z \approx 5$ (b)$R_A/R_Z \approx 1$ (c)$R_A/R_Z \approx 0.2$

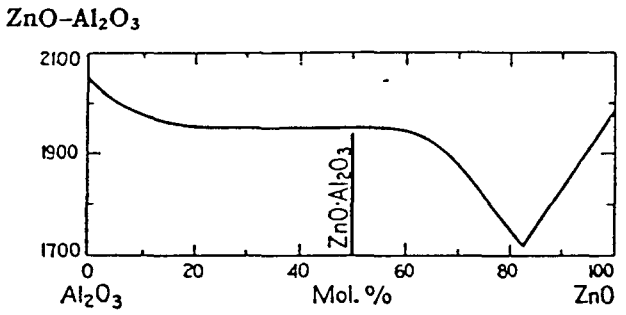

Figure 1

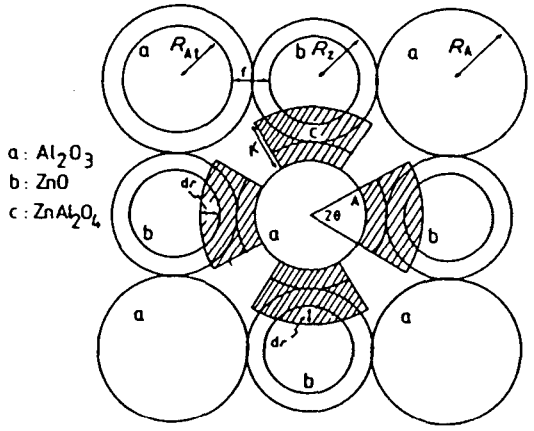

Figure 2

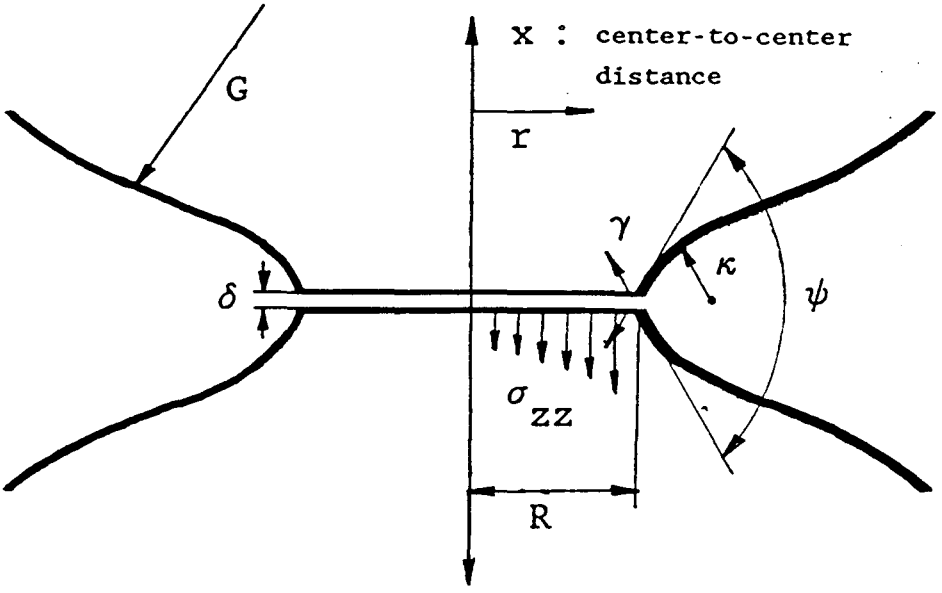

Figure 3

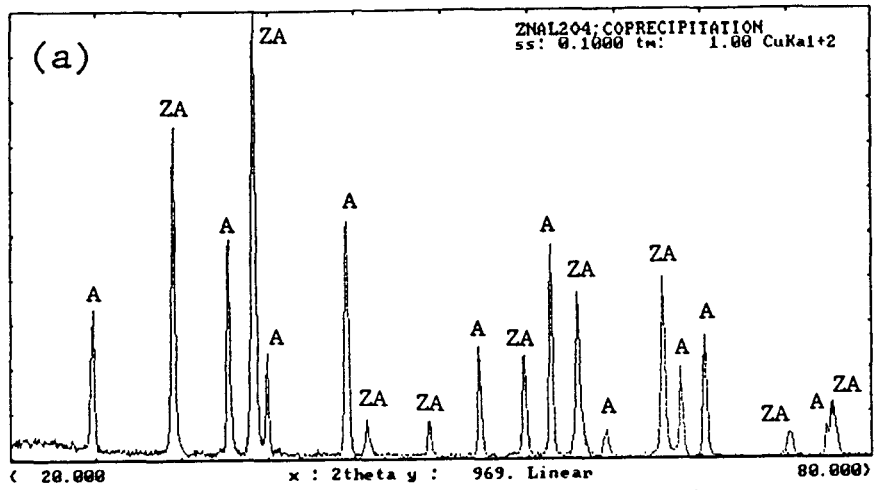
(a)
ZNAL204;COPRECIPITATION
ss: 0.1000 tm: 1.00 CuKa1+2
ZA
ZA
A
A
A
A
ZA
ZA
A
ZA
A
A
ZA
ZA
A
A
ZA
A
ZA
(20.000
x : 2theta y : 969. Linear
80.000)

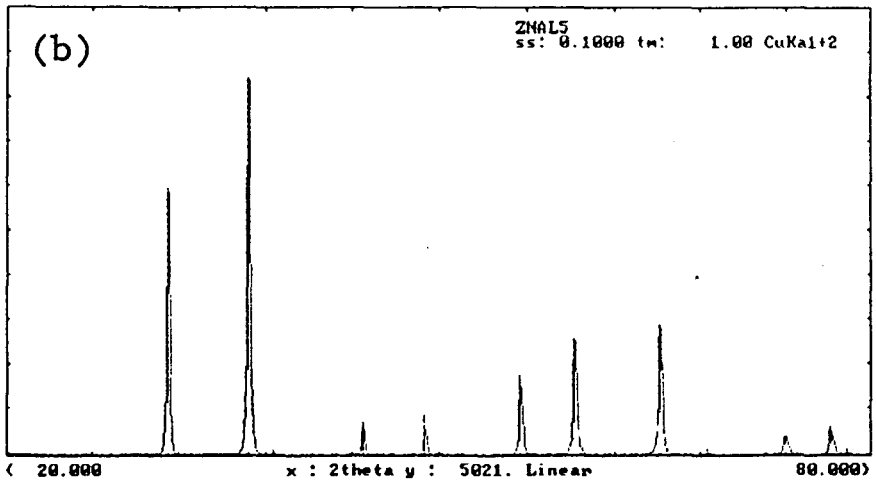
(b)
ZNAL5
ss: 0.1000 tm: 1.00 CuKa1+2
(20.000
x : 2theta y : 5021. Linear
80.000)

Figure 4

Figure 5

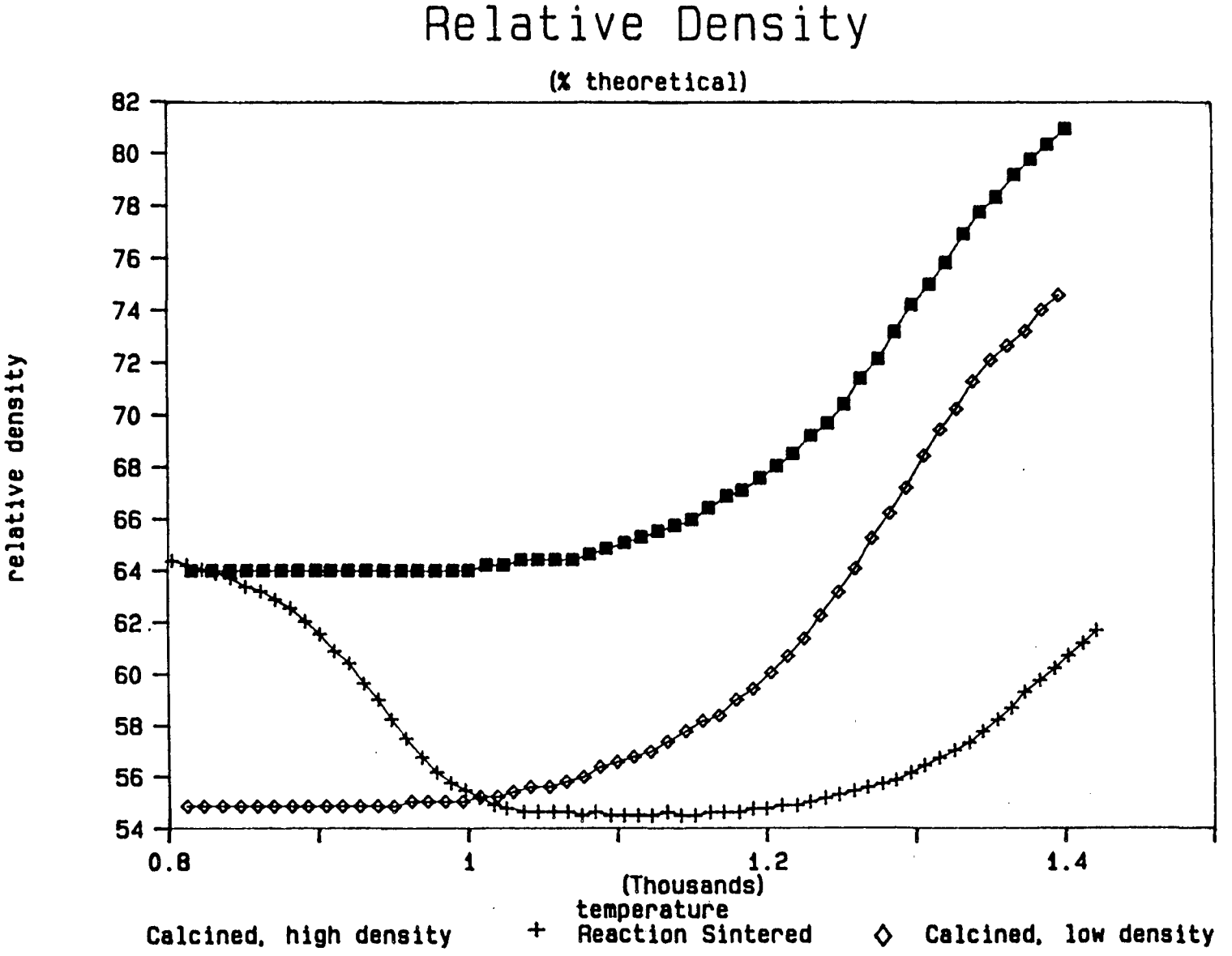
Relative Density
(% theoretical)
relative density
82
80
78
76
74
72
70
68
66
64
62
60
58
56
54
0.8
1
1.2
1.4
(Thousands)
temperature
Calcined, high density
Reaction Sintered
Calcined, low density

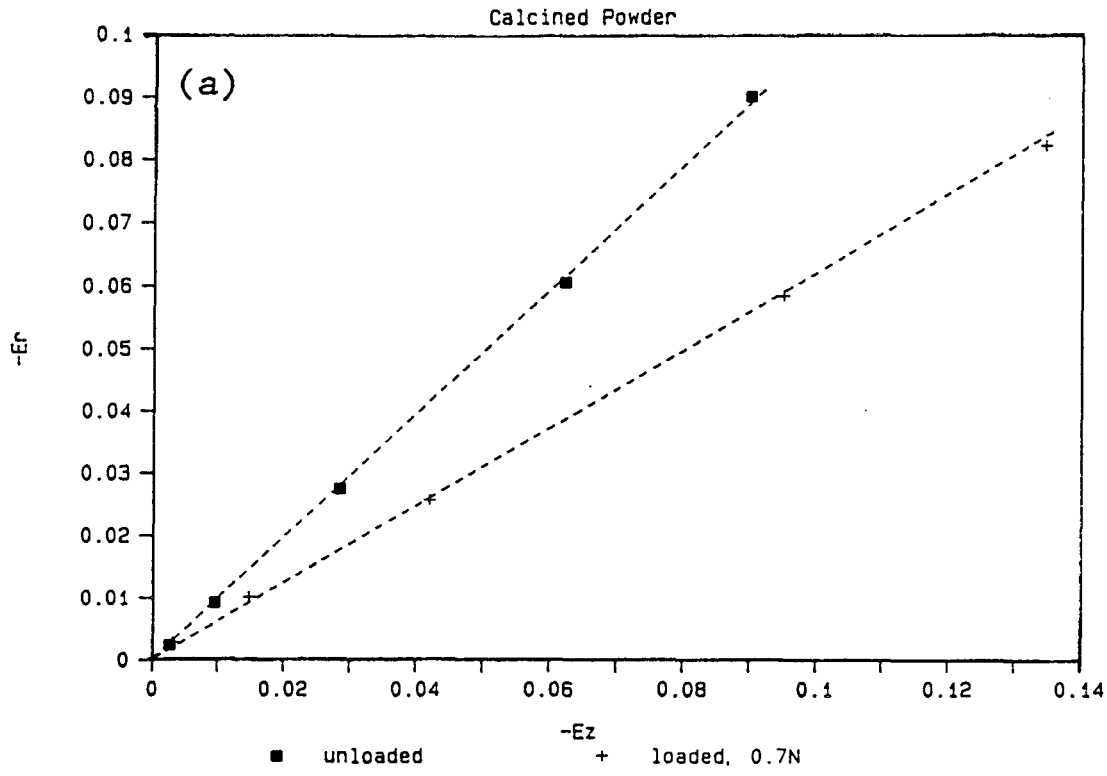
Radial Strain vs. Axial Strain
Calcined Powder
(a)
-Er
-Ez
unloaded
loaded, 0.7N

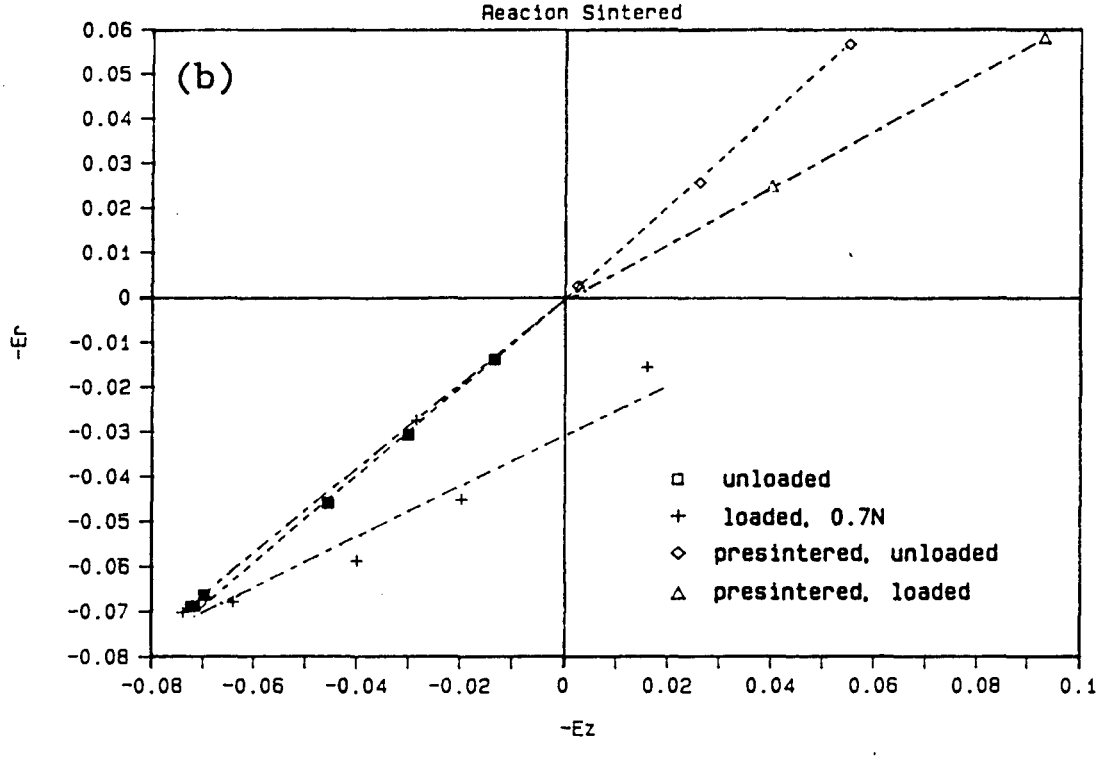
Reacion Sintered
(b)
-Er
-Ez
unloaded
loaded, 0.7N
presintered, unloaded
presintered, loaded

Figure 6

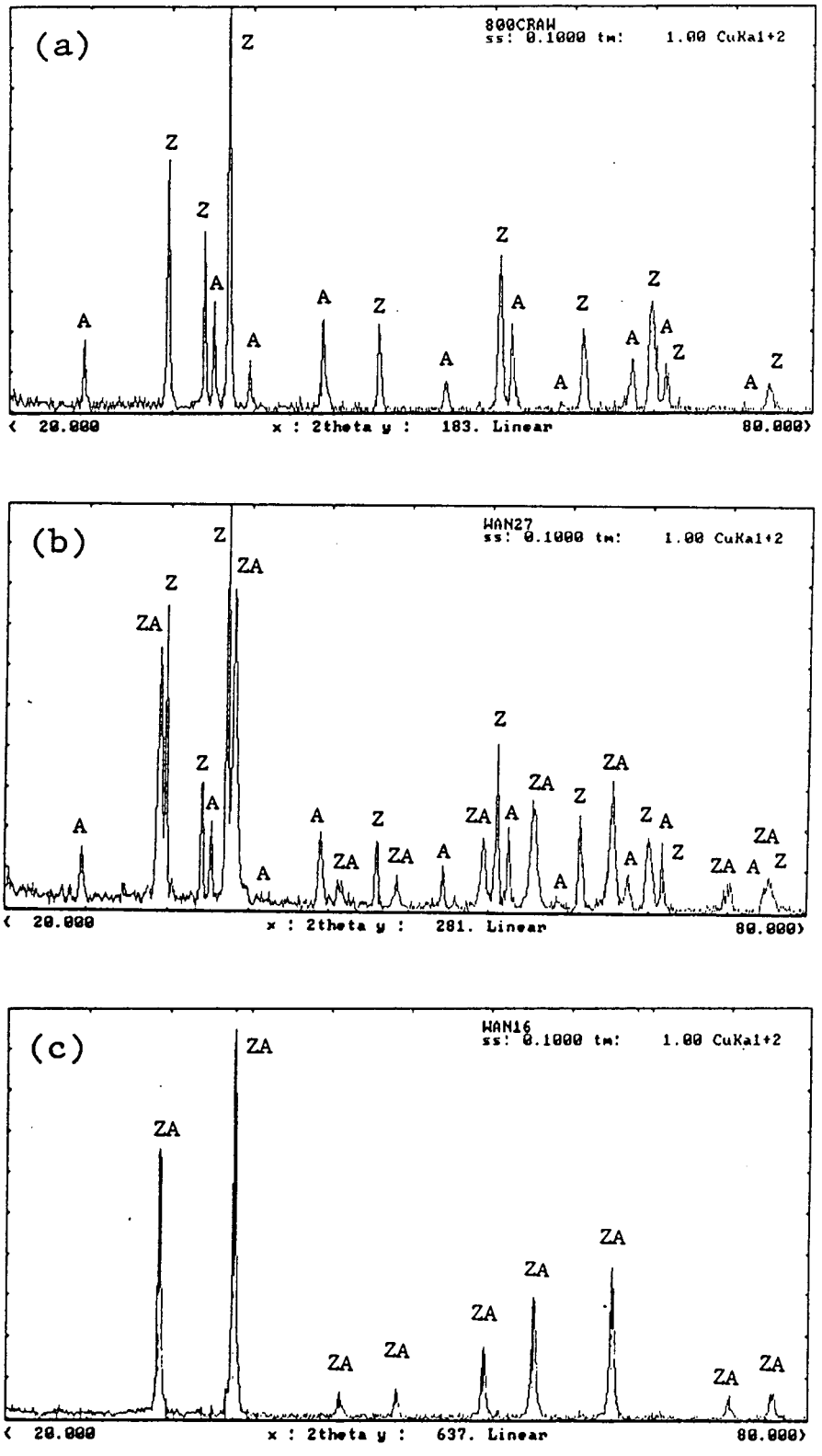
(a)
800CRAW
ss: 0.1000 tm: 1.00 CuKa1+2
x : 2theta y : 183. Linear
(b)
WAN27
ss: 0.1000 tm: 1.00 CuKa1+2
x : 2theta y : 281. Linear
(c)
WAN16
ss: 0.1000 tm: 1.00 CuKa1+2
x : 2theta y : 637. Linear

Figure 7

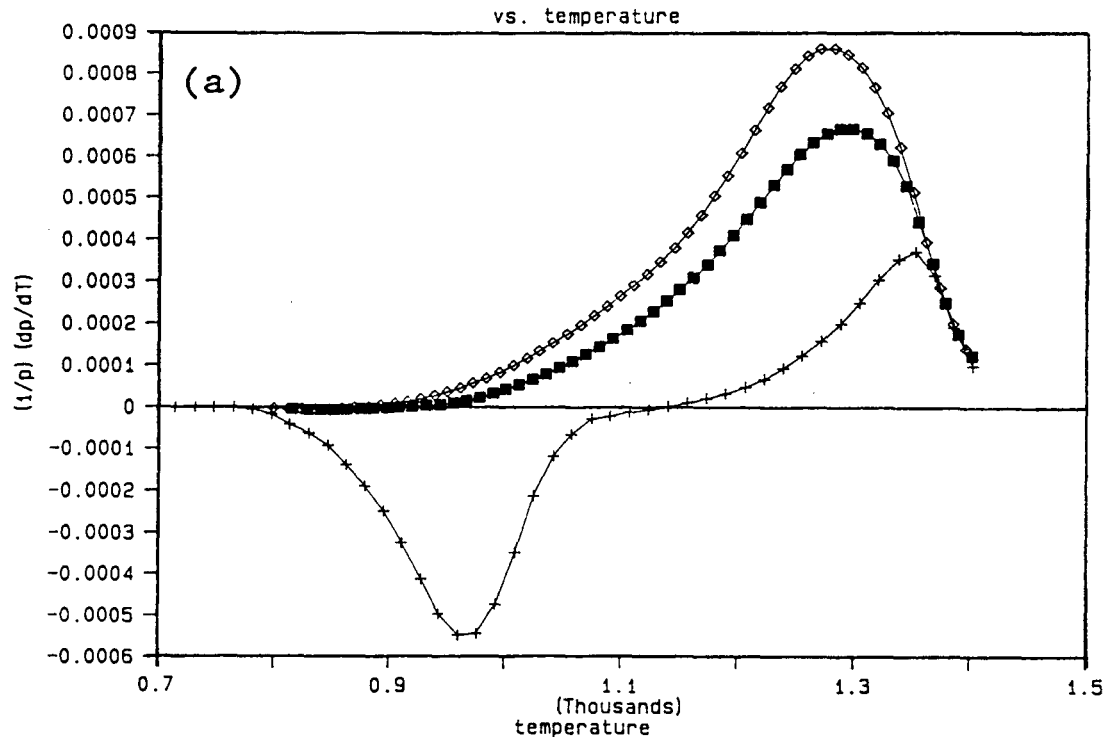
Temperature Derivative of Densification Strain
vs. temperature
(a)
(1/p) (dp/dT)
0.0009
0.0008
0.0007
0.0006
0.0005
0.0004
0.0003
0.0002
0.0001
0
-0.0001
-0.0002
-0.0003
-0.0004
-0.0005
-0.0006
0.7
0.9
1.1
1.3
1.5
(Thousands)
temperature

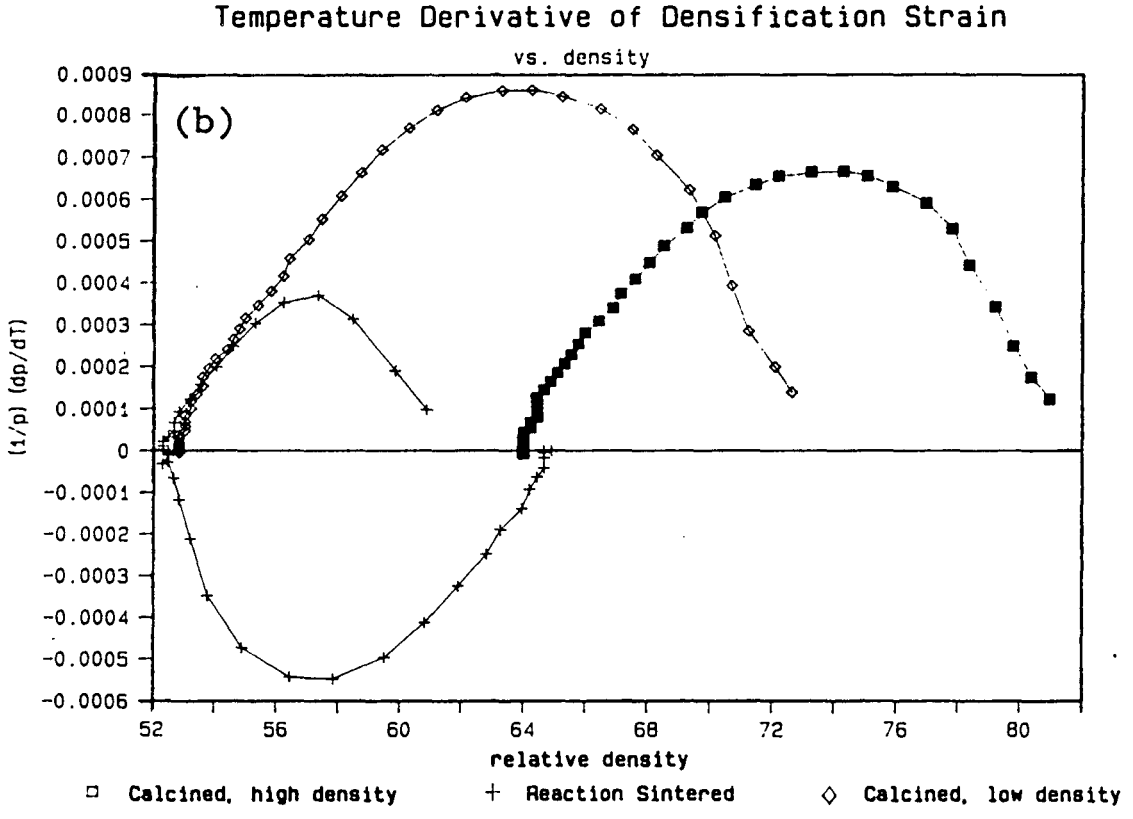
Temperature Derivative of Densification Strain
vs. density
(b)
(1/p) (dp/dT)
0.0009
0.0008
0.0007
0.0006
0.0005
0.0004
0.0003
0.0002
0.0001
0
-0.0001
-0.0002
-0.0003
-0.0004
-0.0005
-0.0006
52
56
60
64
68
72
76
80
relative density
Calcined, high density
Reaction Sintered
Calcined, low density

Figure 8

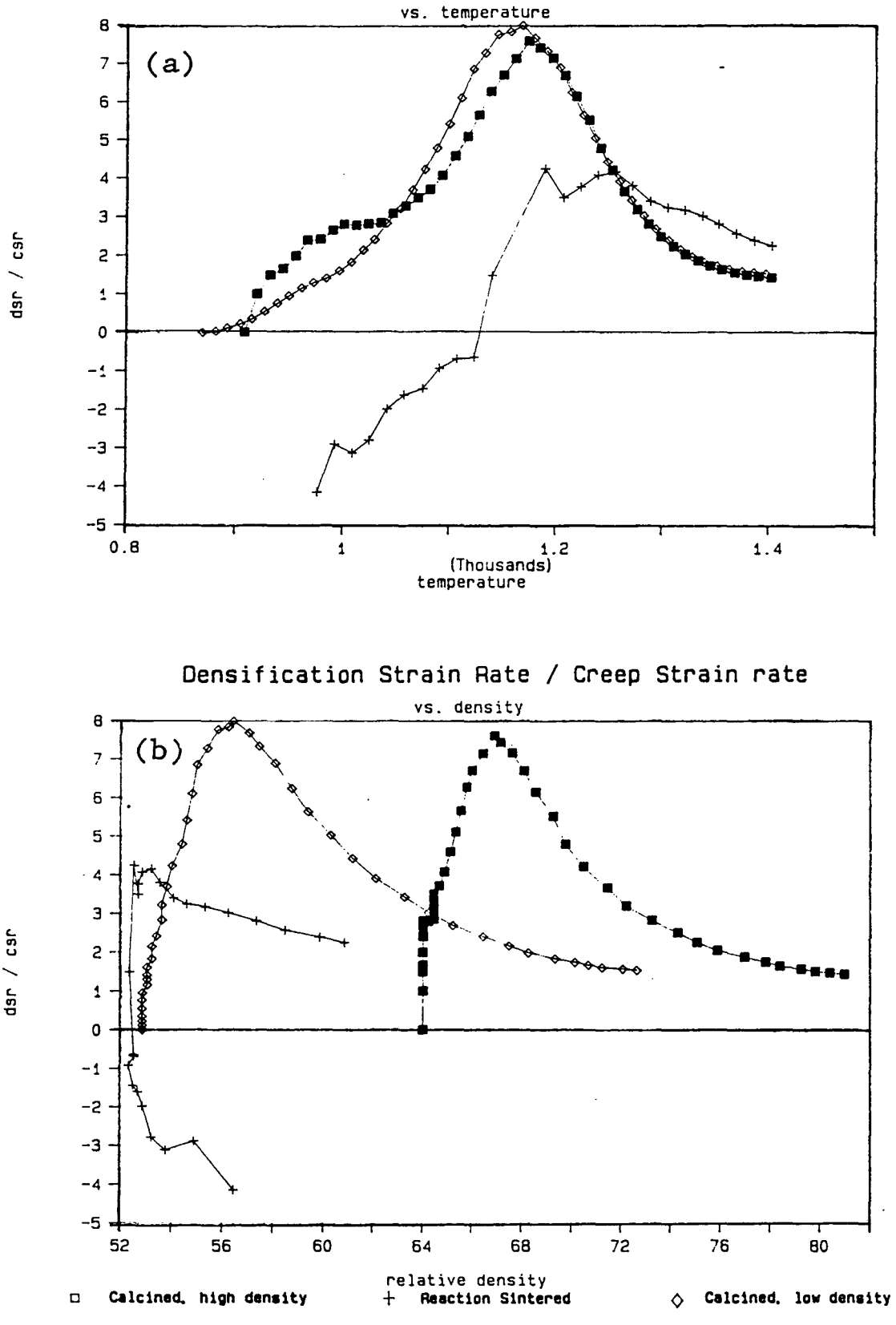
Densification Strain Rate / Creep Strain Rate
vs. temperature
(a)
dsr / csr
8
7
6
5
4
3
2
1
0
-1
-2
-3
-4
-5
0.8
1
1.2
1.4
(Thousands)
temperature
Densification Strain Rate / Creep Strain rate
vs. density
(b)
dsr / csr
8
7
6
5
4
3
2
1
0
-1
-2
-3
-4
-5
52
56
60
64
68
72
76
80
relative density
□ Calcined, high density
+ Reaction Sintered
◇ Calcined, low density

Figure 9

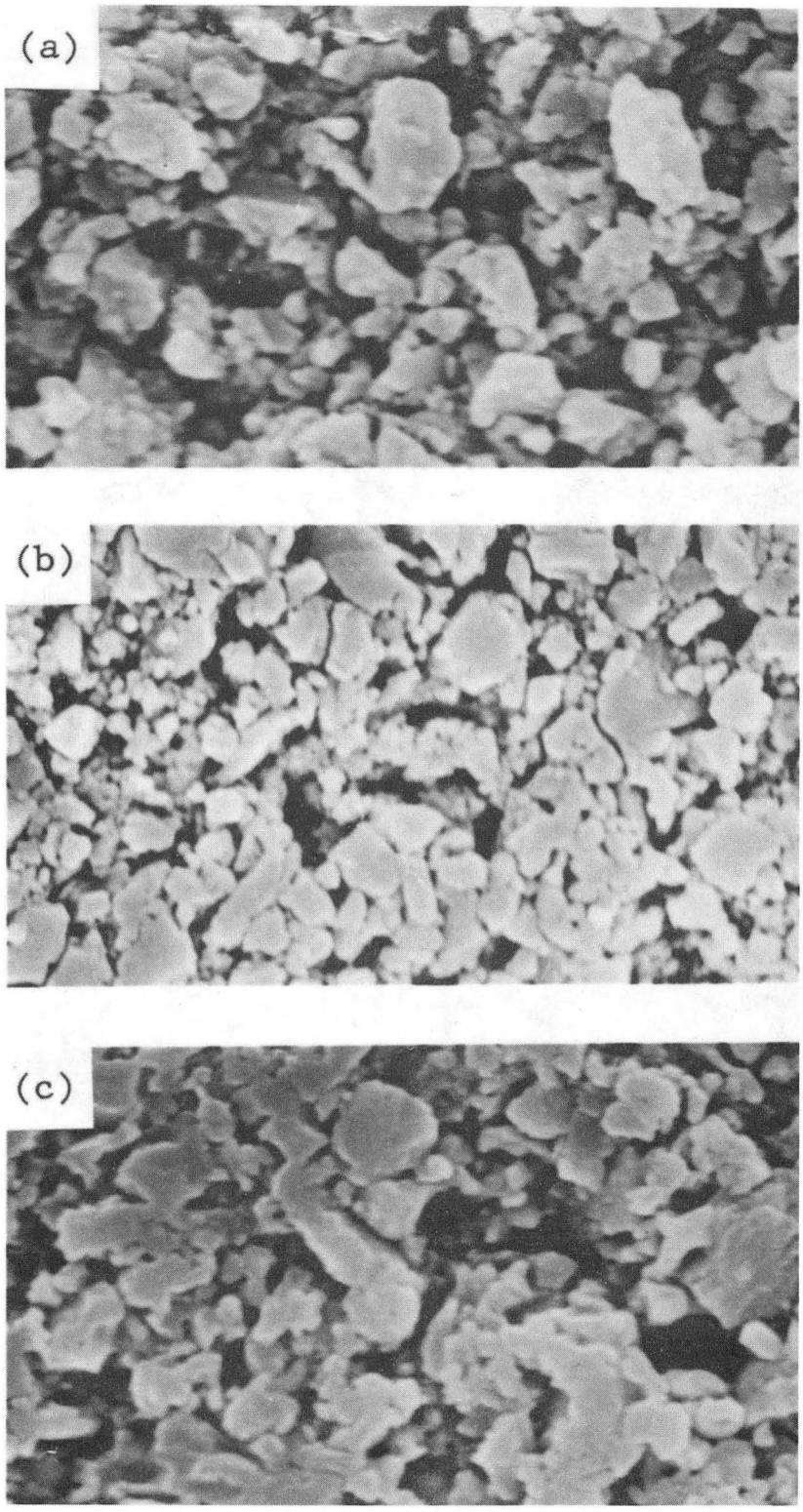

XBB 915-3636

1 μm

Figure 10

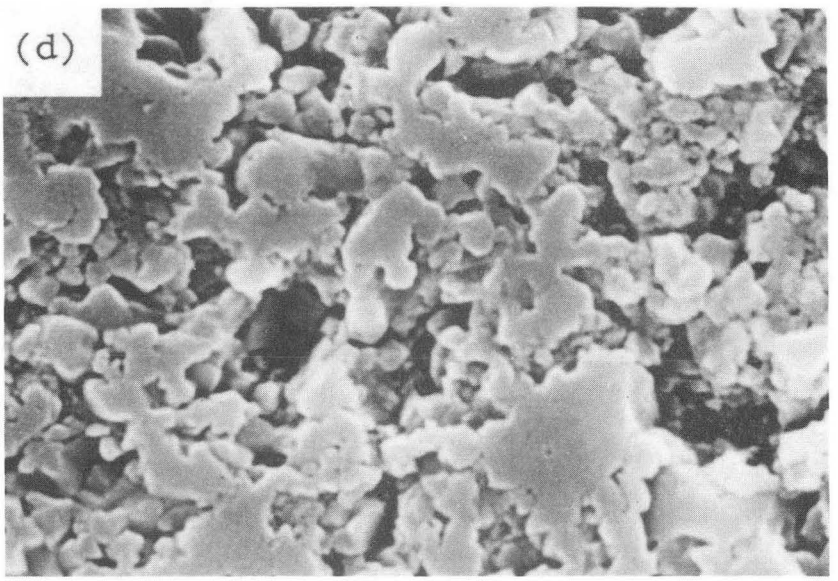

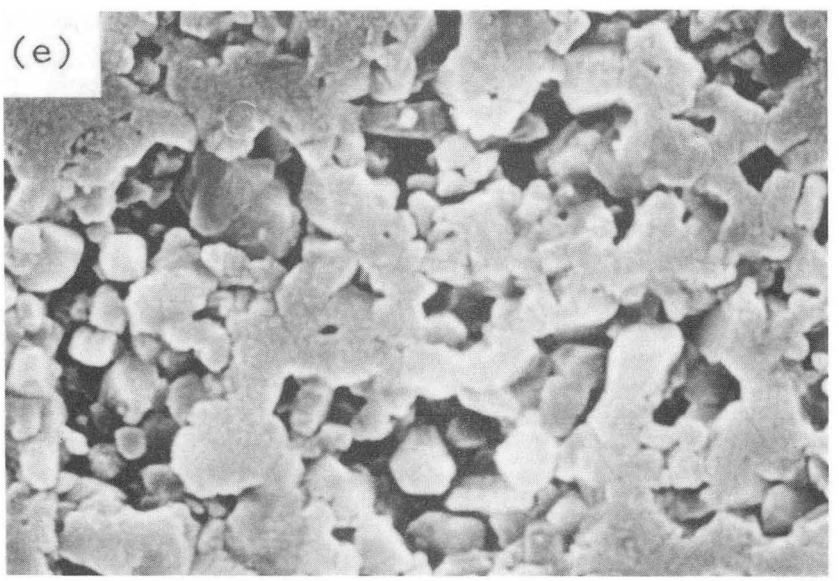

XBB 915-3637

1 μm

Figure 10 (Continued)

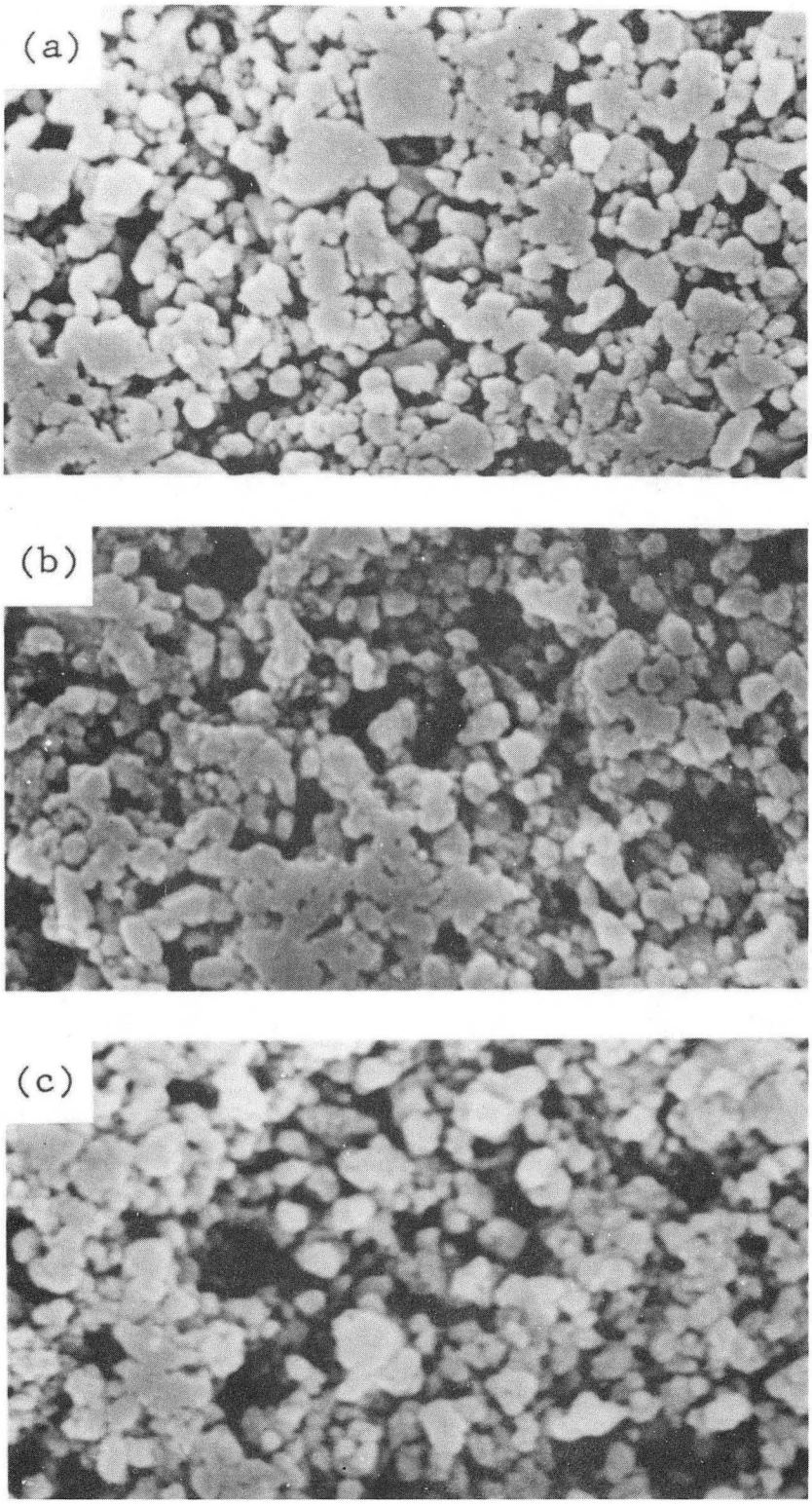

XBB 915-3638

1μm

Figure 11

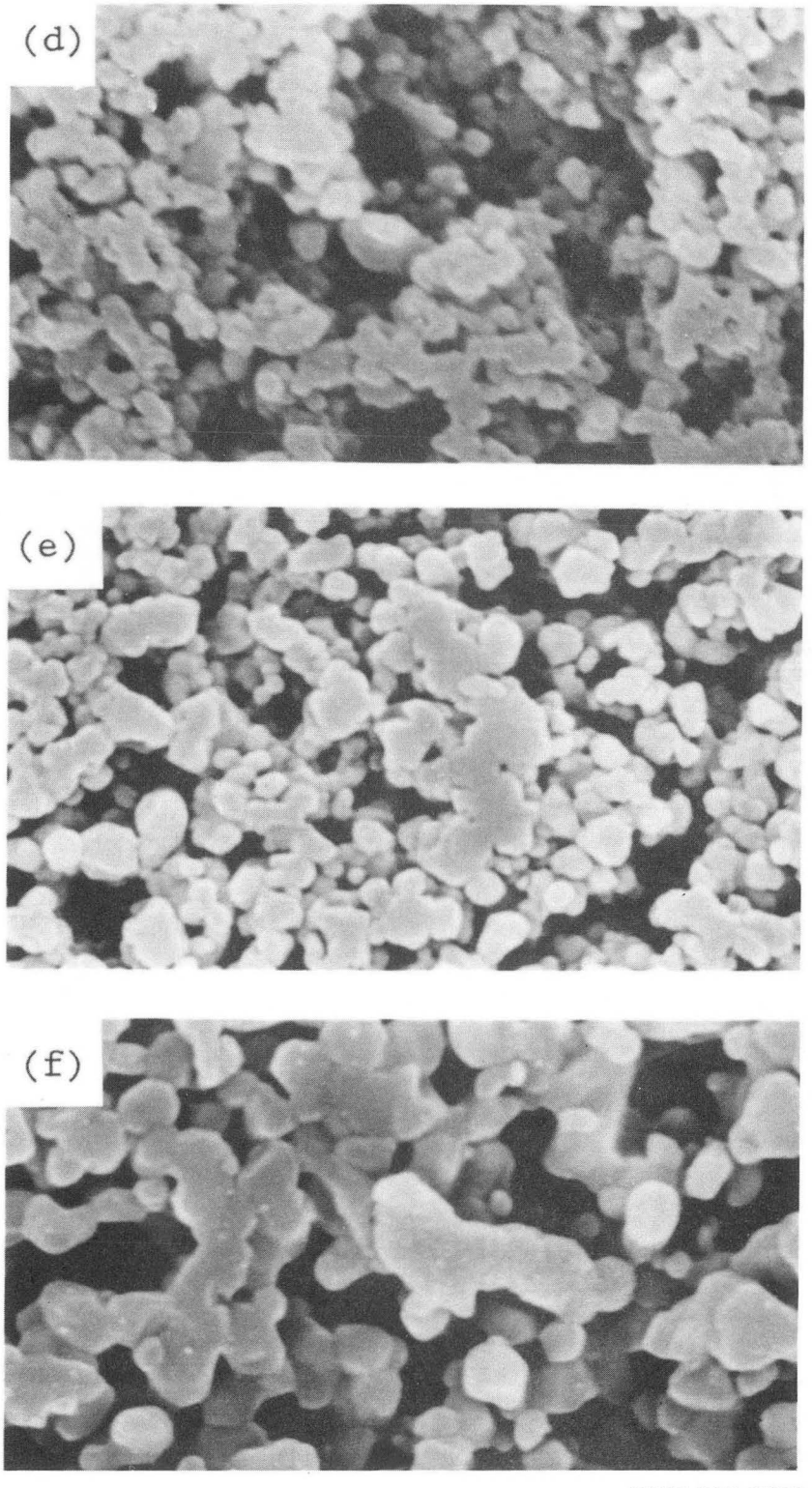

Figure 11 (continued)

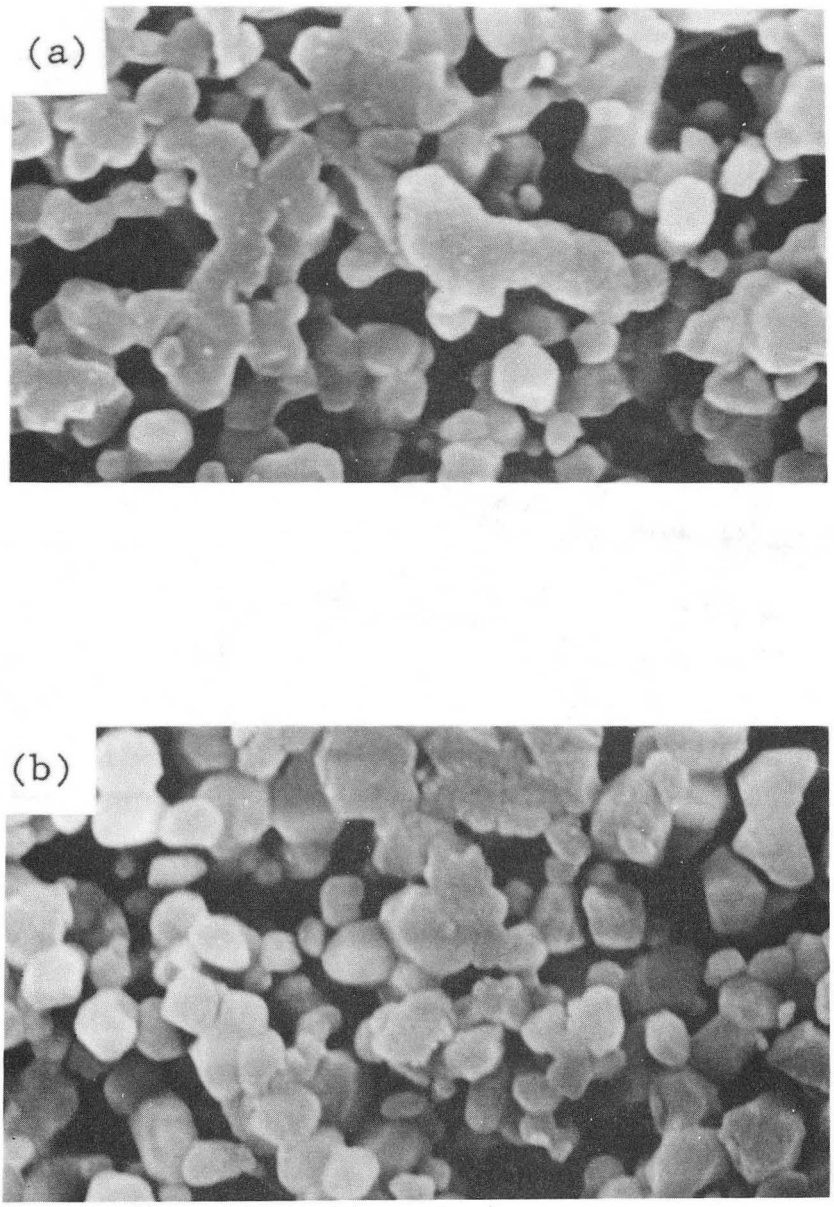

XBB 915-3640

1μm

Figure 12

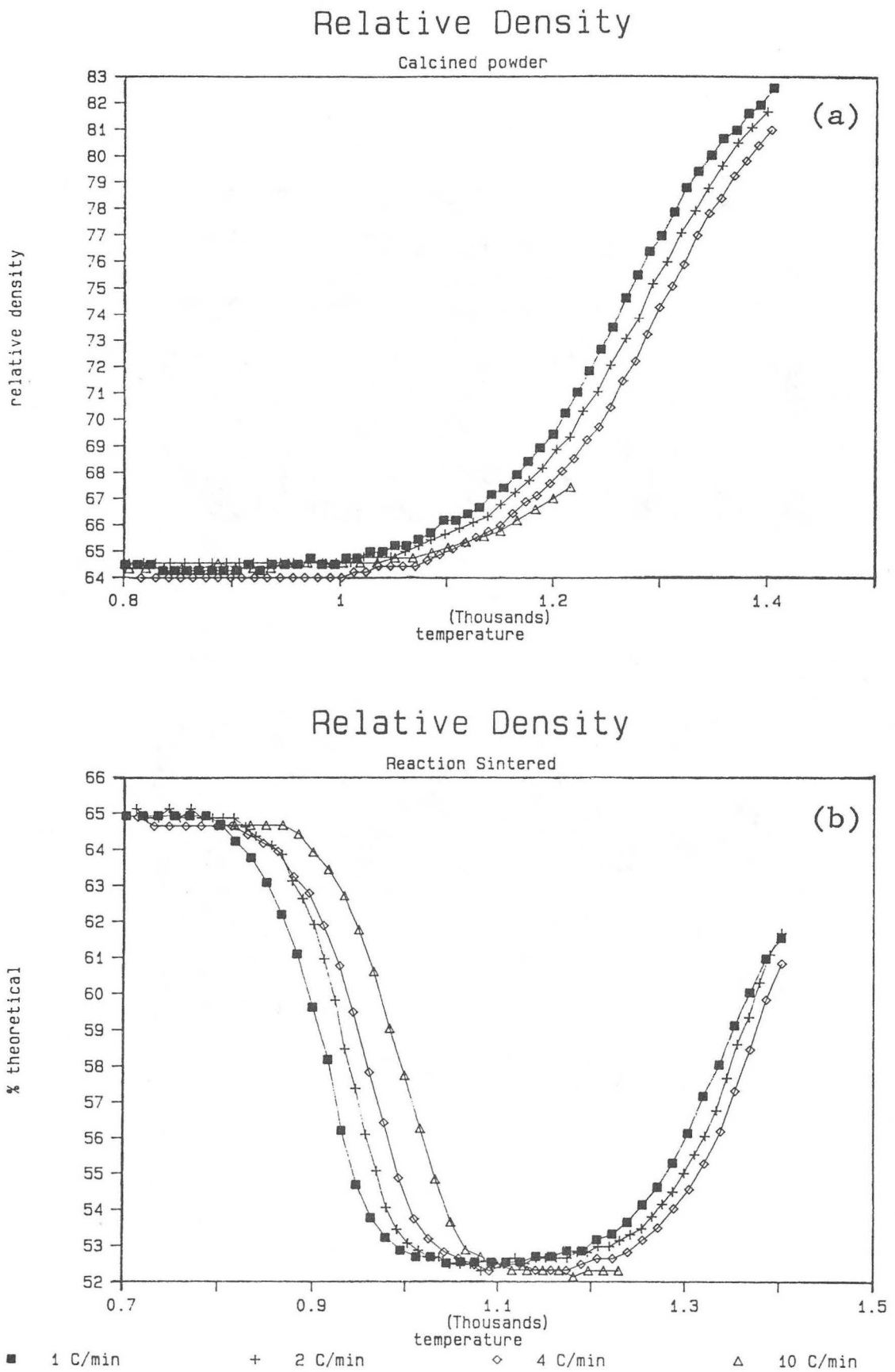
Relative Density
Calcined powder
(a)
relative density
83
82
81
80
79
78
77
76
75
74
73
72
71
70
69
68
67
66
65
64
0.8
1
1.2
1.4
(Thousands)
temperature
Relative Density
Reaction Sintered
(b)
% theoretical
66
65
64
63
62
61
60
59
58
57
56
55
54
53
52
0.7
0.9
1.1
1.3
1.5
(Thousands)
temperature
1 C/min
2 C/min
4 C/min
10 C/min

Figure 13

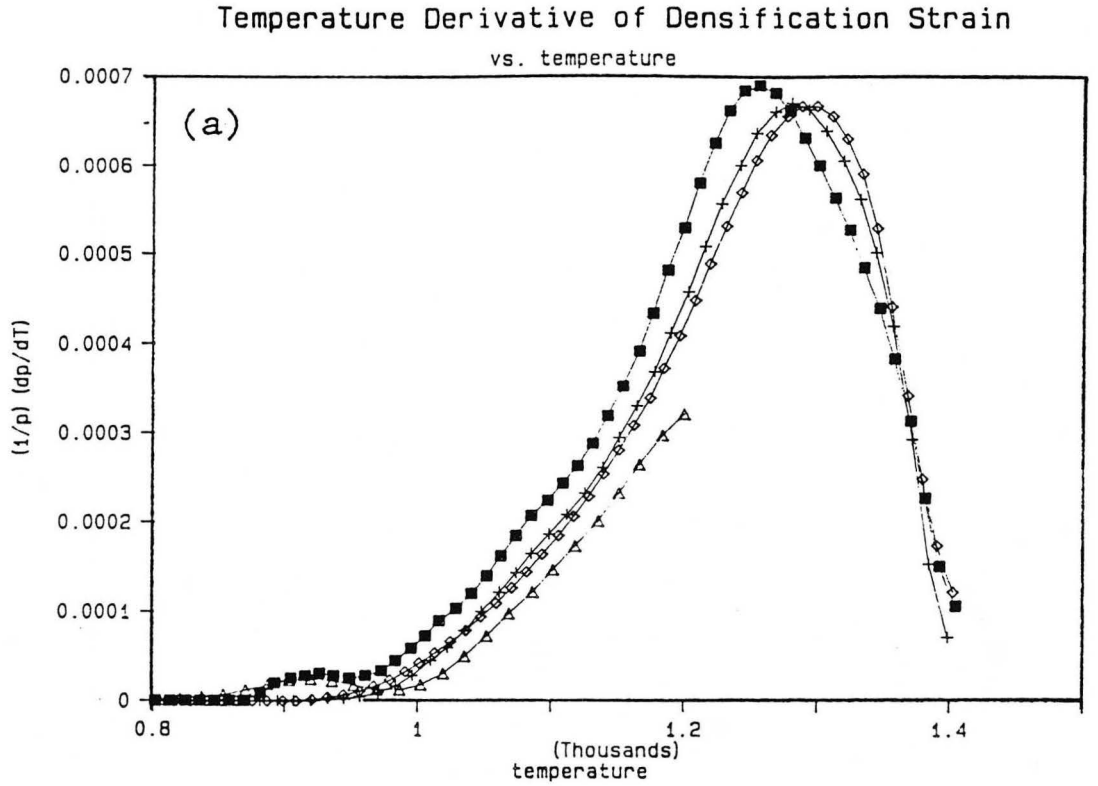
Temperature Derivative of Densification Strain
vs. temperature
(a)
0.0007
0.0006
0.0005
0.0004
0.0003
0.0002
0.0001
0
(1/p) (dp/dT)
0.8
1
1.2
1.4
(Thousands)
temperature

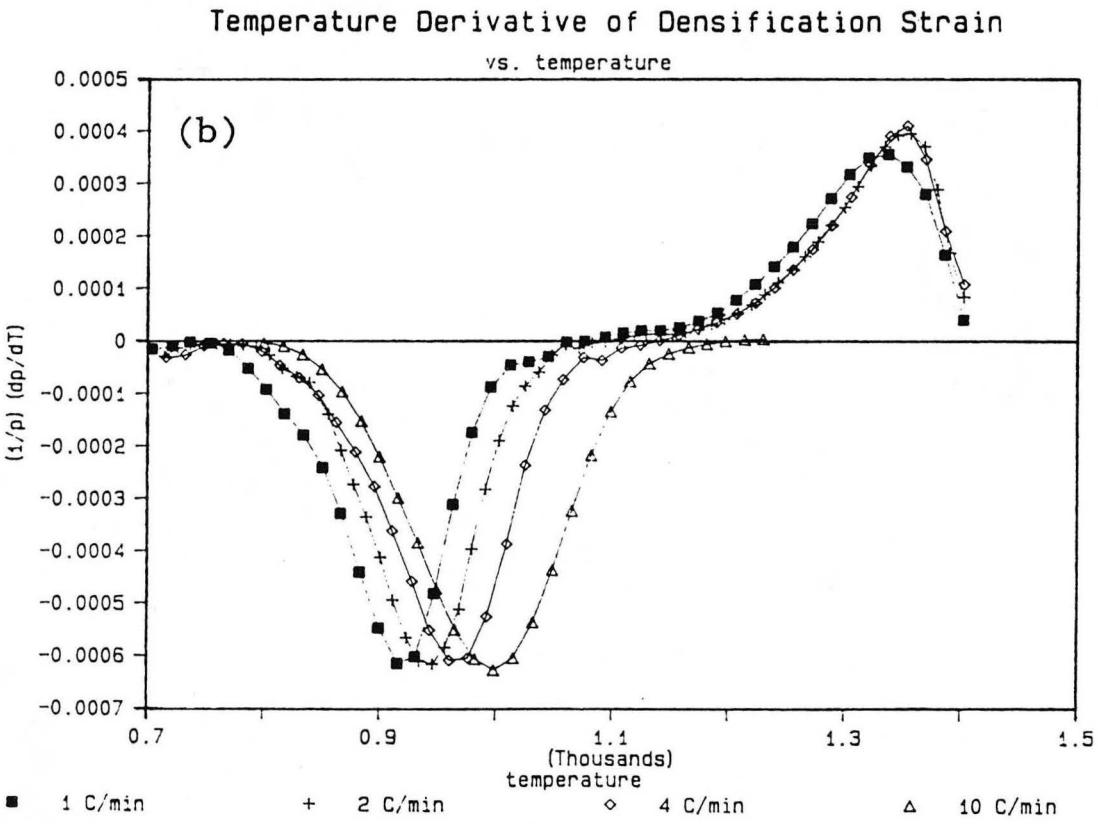
Temperature Derivative of Densification Strain
vs. temperature
(b)
0.0005
0.0004
0.0003
0.0002
0.0001
0
-0.0001
-0.0002
-0.0003
-0.0004
-0.0005
-0.0006
-0.0007
(1/p) (dp/dT)
0.7
0.9
1.1
1.3
1.5
(Thousands)
temperature
1 C/min
2 C/min
4 C/min
10 C/min

Figure 14

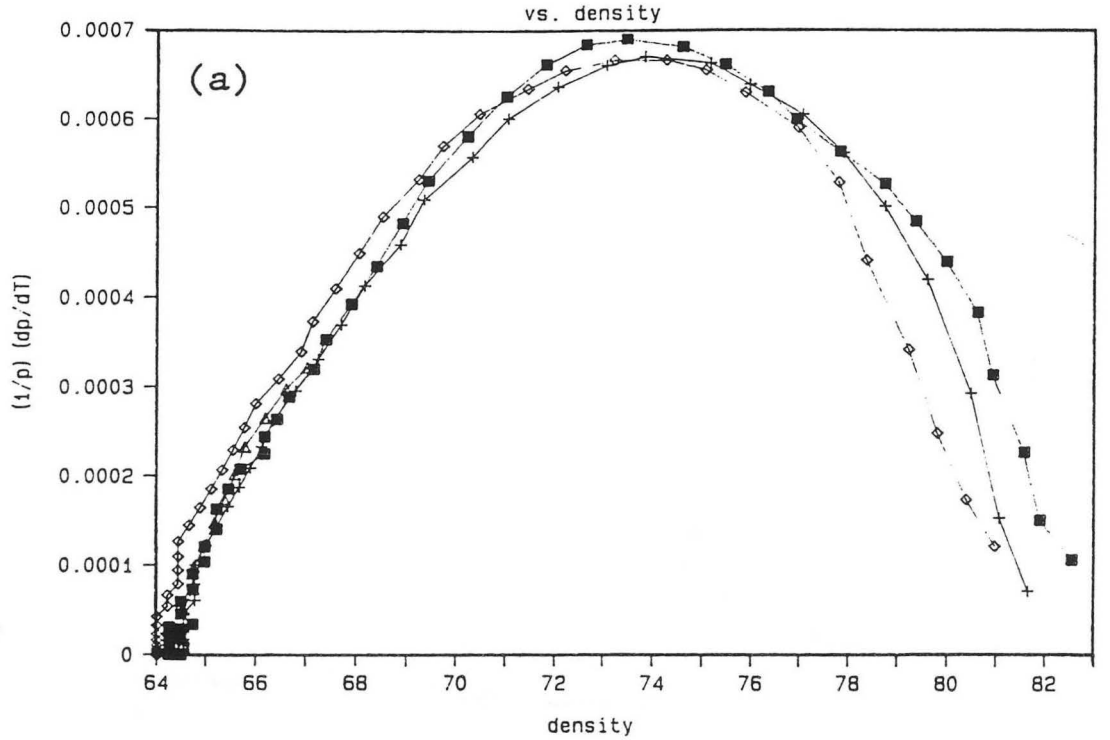
Temperature Derivative of Densification Strain
vs. density
(a)
0.0007
0.0006
0.0005
0.0004
0.0003
0.0002
0.0001
0
(1/ρ) (dρ/dT)
64
66
68
70
72
74
76
78
80
82
density

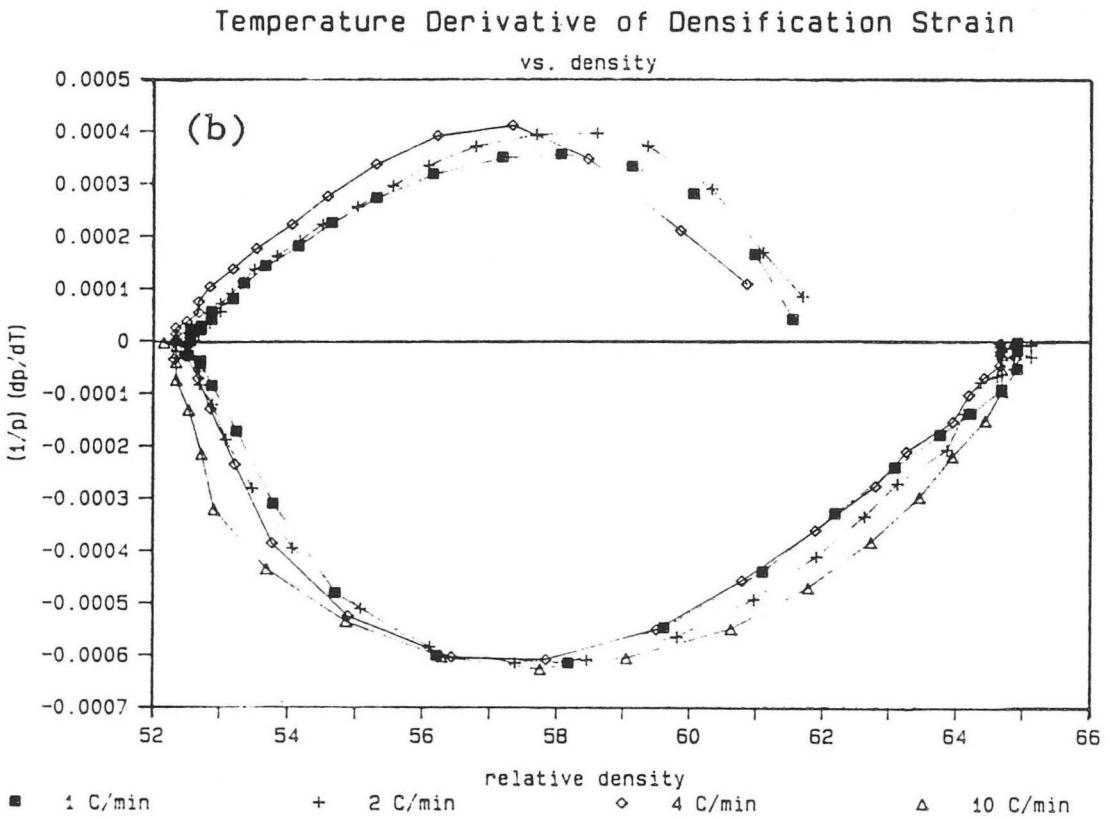
Temperature Derivative of Densification Strain
vs. density
(b)
0.0005
0.0004
0.0003
0.0002
0.0001
0
-0.0001
-0.0002
-0.0003
-0.0004
-0.0005
-0.0006
-0.0007
(1/ρ) (dρ/dT)
52
54
56
58
60
62
64
66
relative density
1 C/min
2 C/min
4 C/min
10 C/min

Figure 15

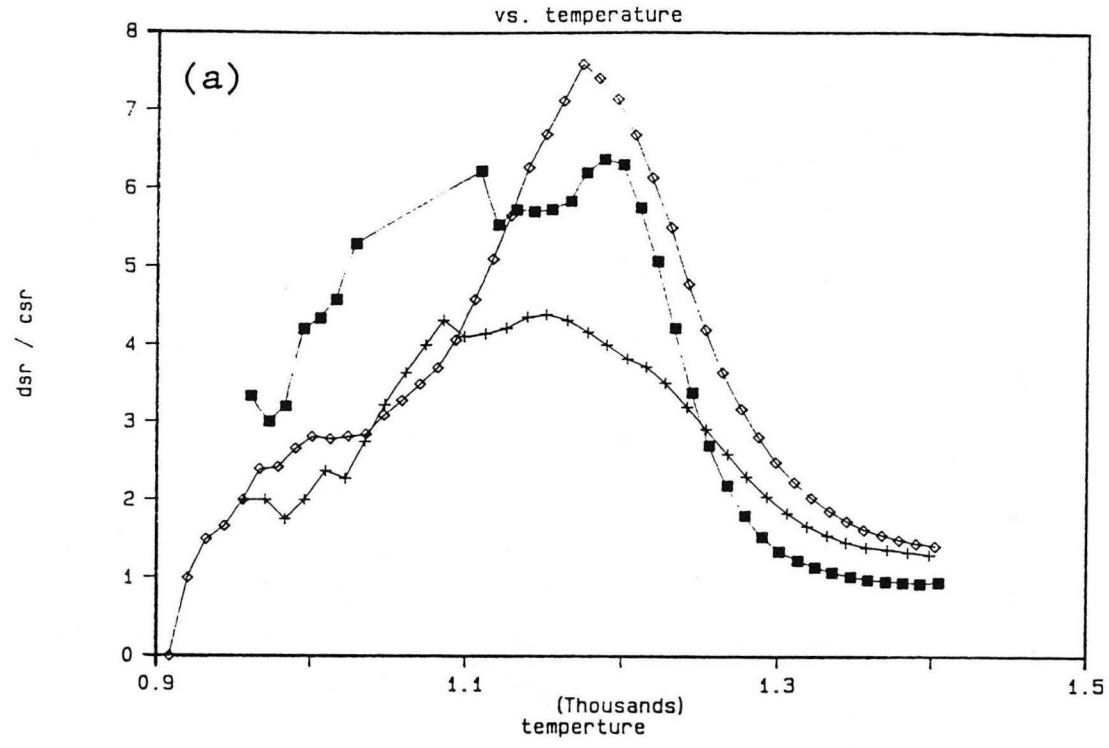
Densification Strain Rate / Creep Strain Rate
vs. temperature
(a)
dsr / csr
8
7
6
5
4
3
2
1
0
0.9
1.1
1.3
1.5
(Thousands)
temperture

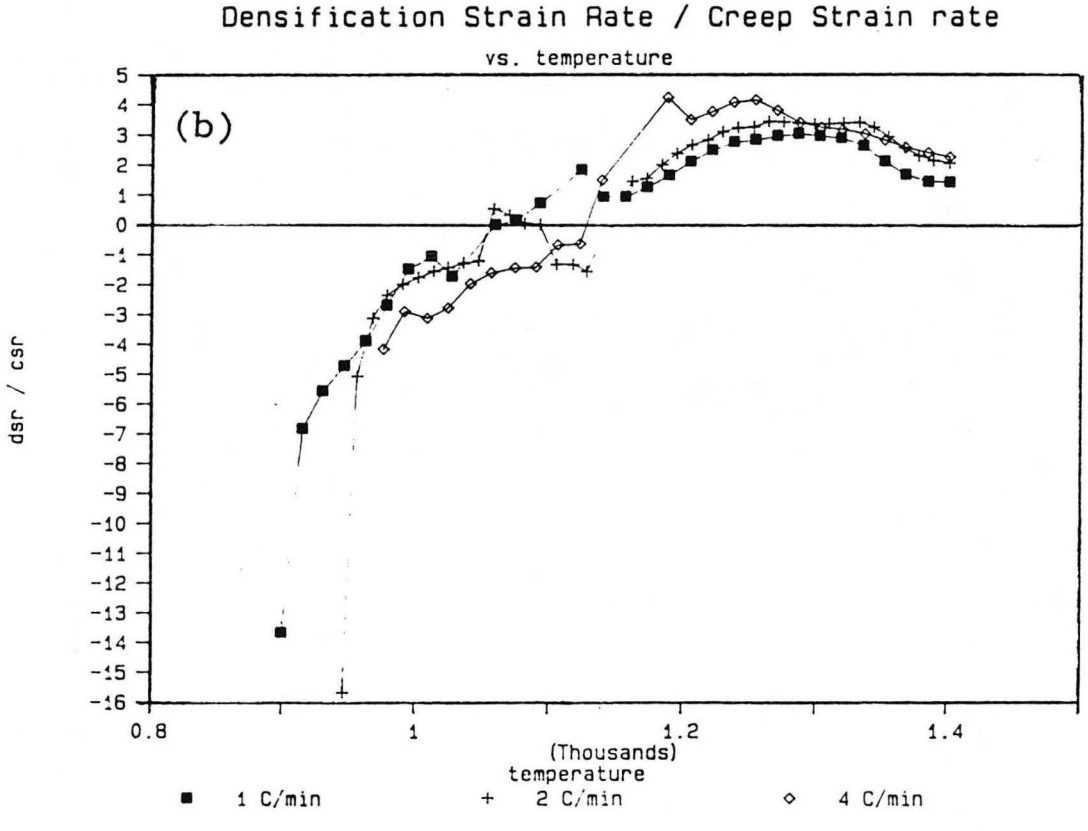
Densification Strain Rate / Creep Strain rate
vs. temperature
(b)
dsr / csr
5
4
3
2
1
0
-1
-2
-3
-4
-5
-6
-7
-8
-9
-10
-11
-12
-13
-14
-15
-16
0.8
1
1.2
1.4
(Thousands)
temperature
1 C/min
2 C/min
4 C/min

Figure 16

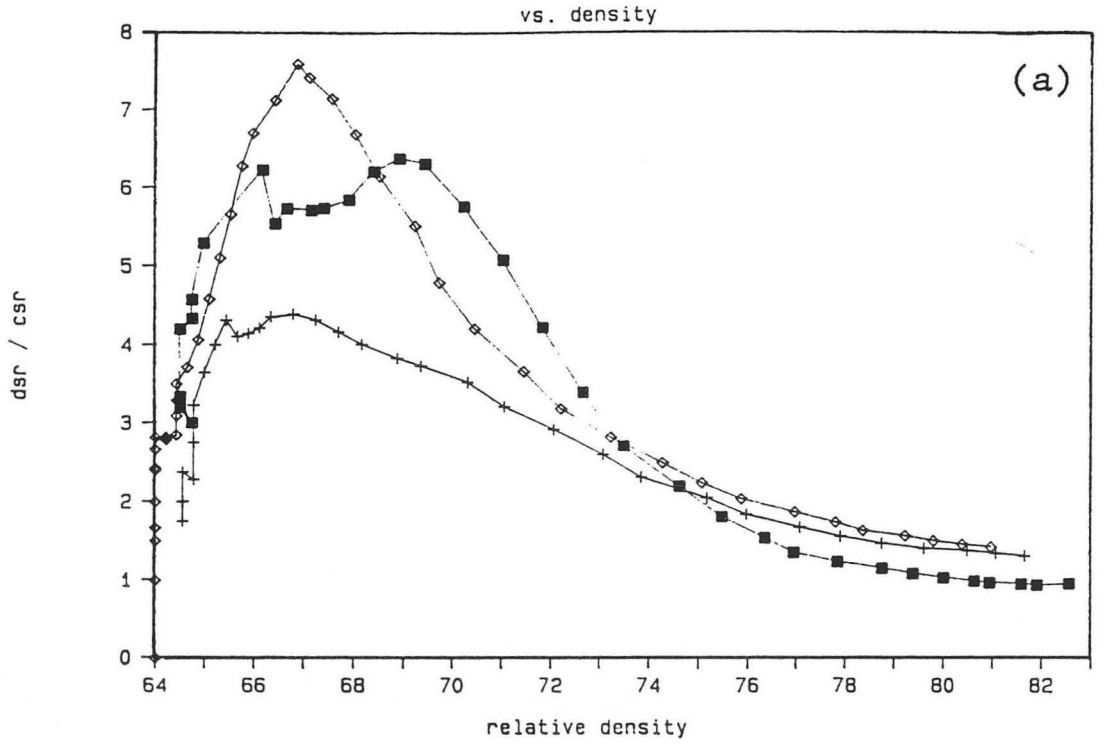
Densification Strain Rate / Creep Strain Rate
vs. density
(a)
dsr / csr
relative density

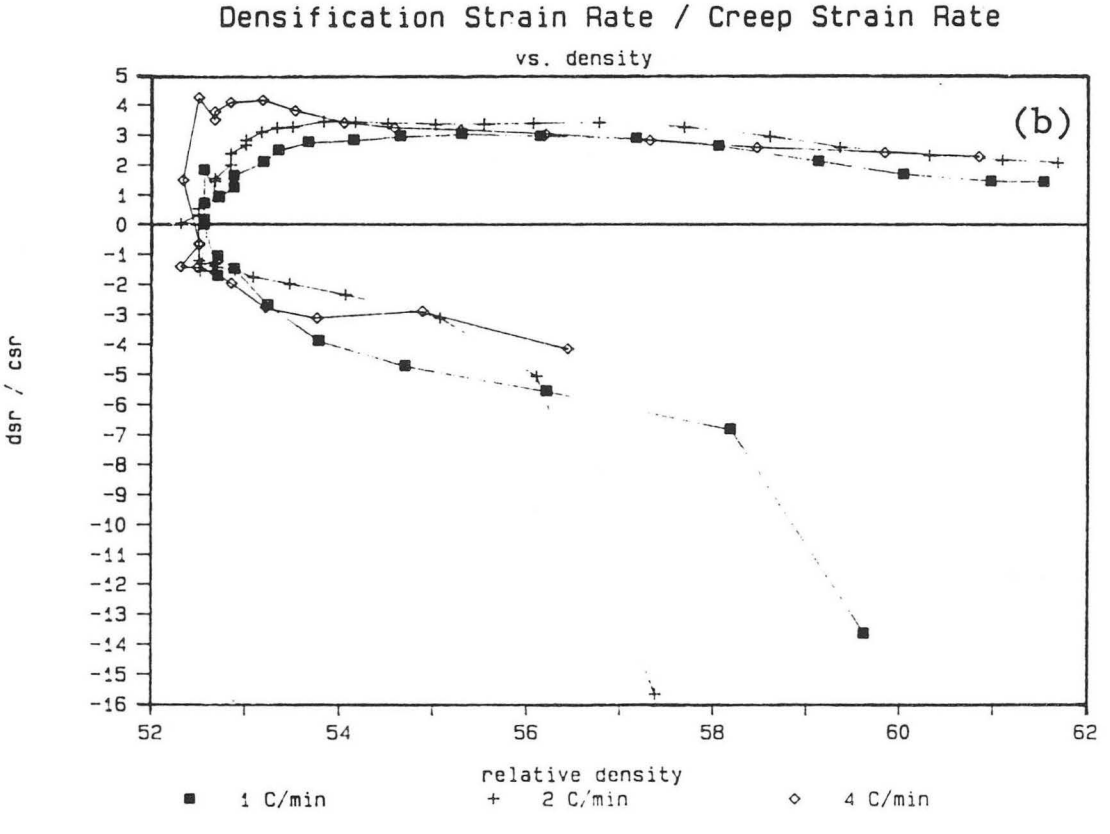
Densification Strain Rate / Creep Strain Rate
vs. density
(b)
dsr / csr
relative density
1 C/min
2 C/min
4 C/min

Figure 17

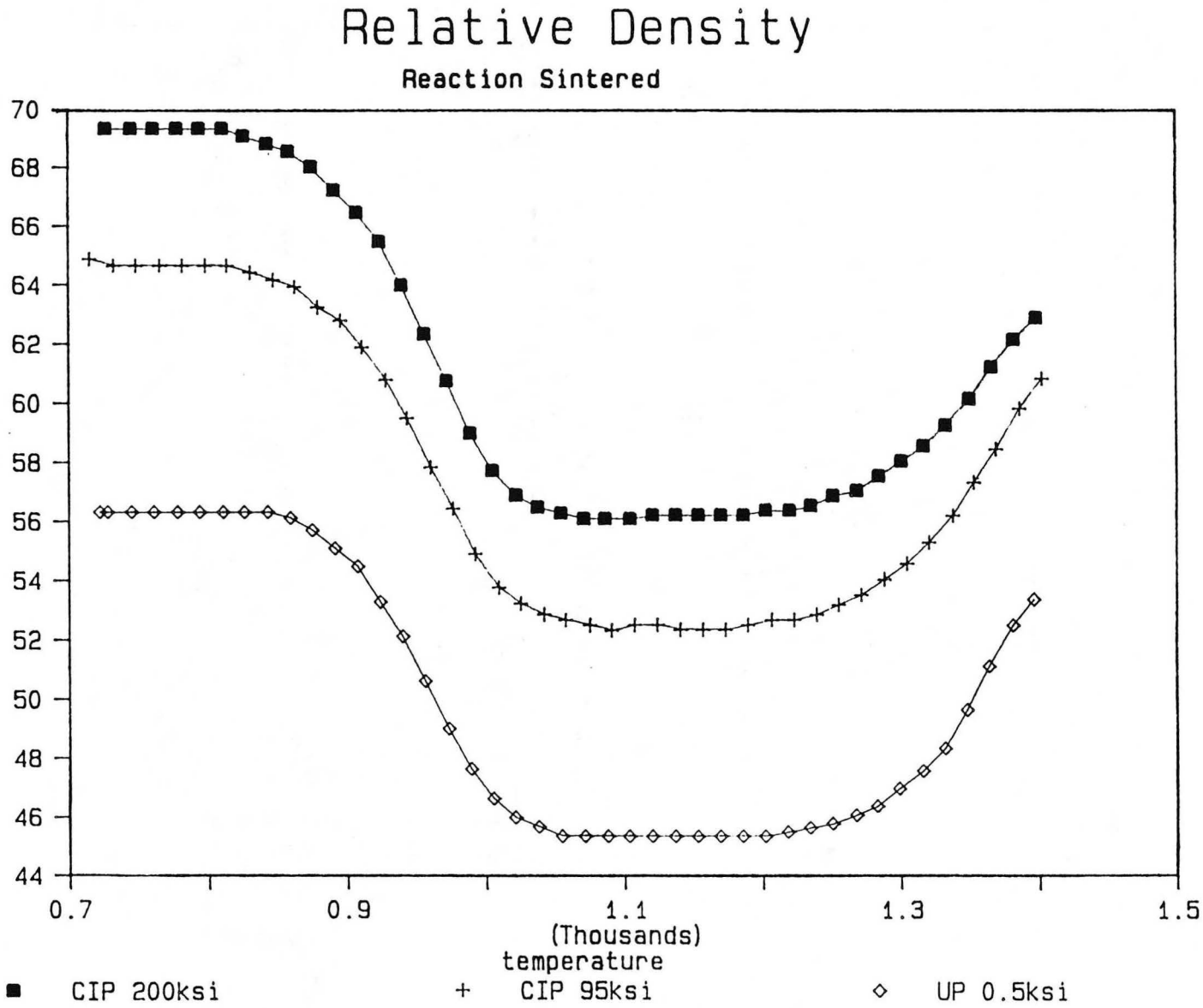
Relative Density
Reaction Sintered
relative density
70
68
66
64
62
60
58
56
54
52
50
48
46
44
0.7
0.9
1.1
1.3
1.5
(Thousands)
temperature
CIP 200ksi
CIP 95ksi
UP 0.5ksi

Figure 18

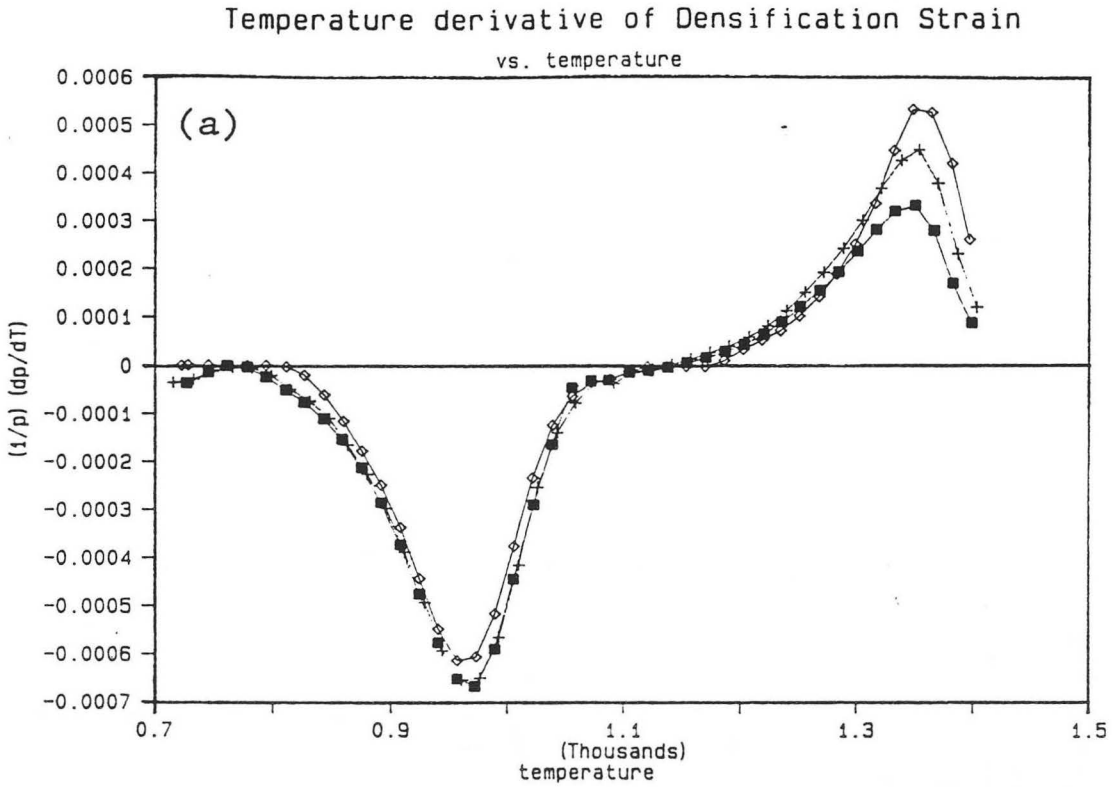
Temperature derivative of Densification Strain
vs. temperature
(a)
(1/p) (dp/dT)
0.0006
0.0005
0.0004
0.0003
0.0002
0.0001
0
-0.0001
-0.0002
-0.0003
-0.0004
-0.0005
-0.0006
-0.0007
0.7
0.9
1.1
1.3
1.5
(Thousands)
temperature

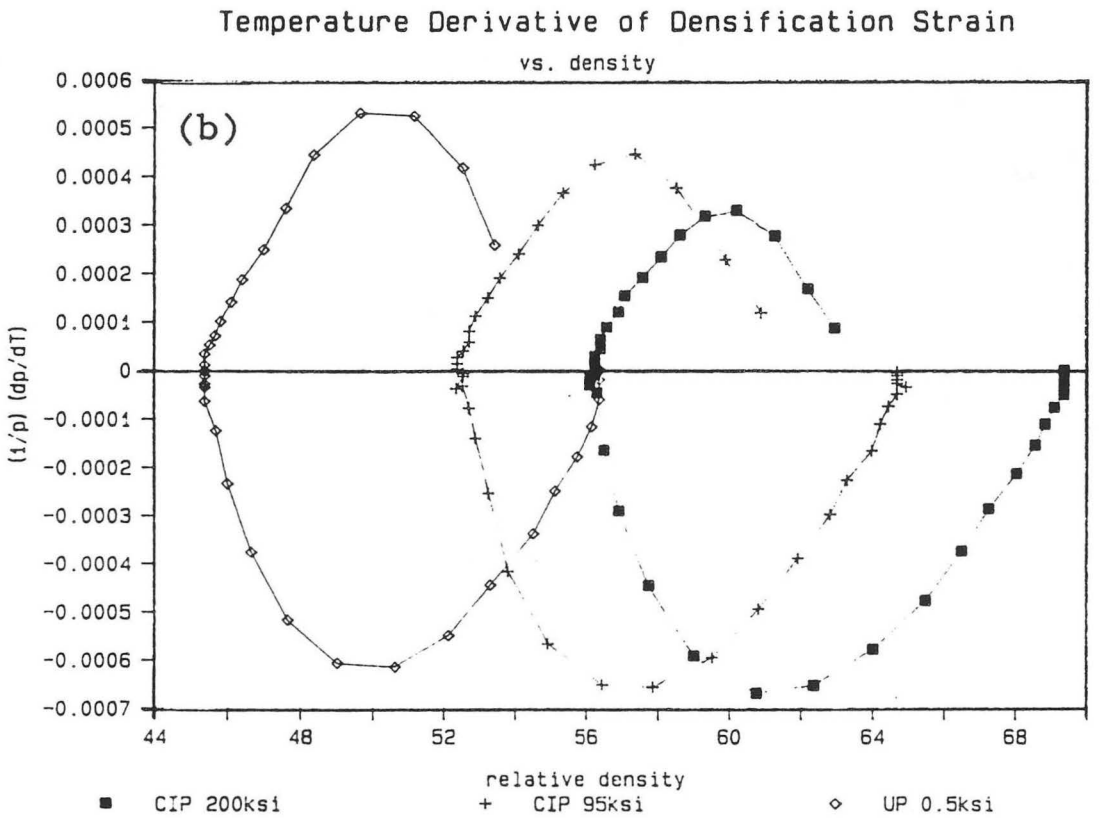
Temperature Derivative of Densification Strain
vs. density
(b)
(1/p) (dp/dT)
0.0006
0.0005
0.0004
0.0003
0.0002
0.0001
0
-0.0001
-0.0002
-0.0003
-0.0004
-0.0005
-0.0006
-0.0007
44
48
52
56
60
64
68
relative density
CIP 200ksi
CIP 95ksi
UP 0.5ksi

Figure 19

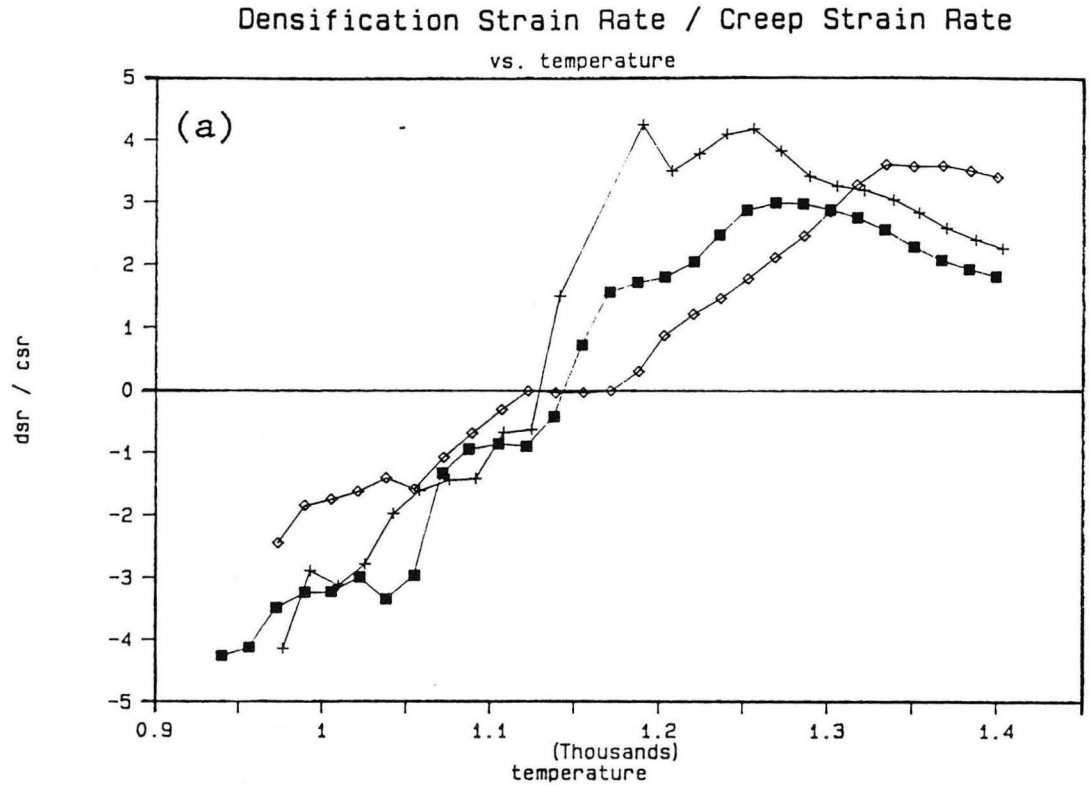
Densification Strain Rate / Creep Strain Rate
vs. temperature
(a)
dsr / csr
5
4
3
2
1
0
-1
-2
-3
-4
-5
0.9
1
1.1
1.2
1.3
1.4
(Thousands)
temperature

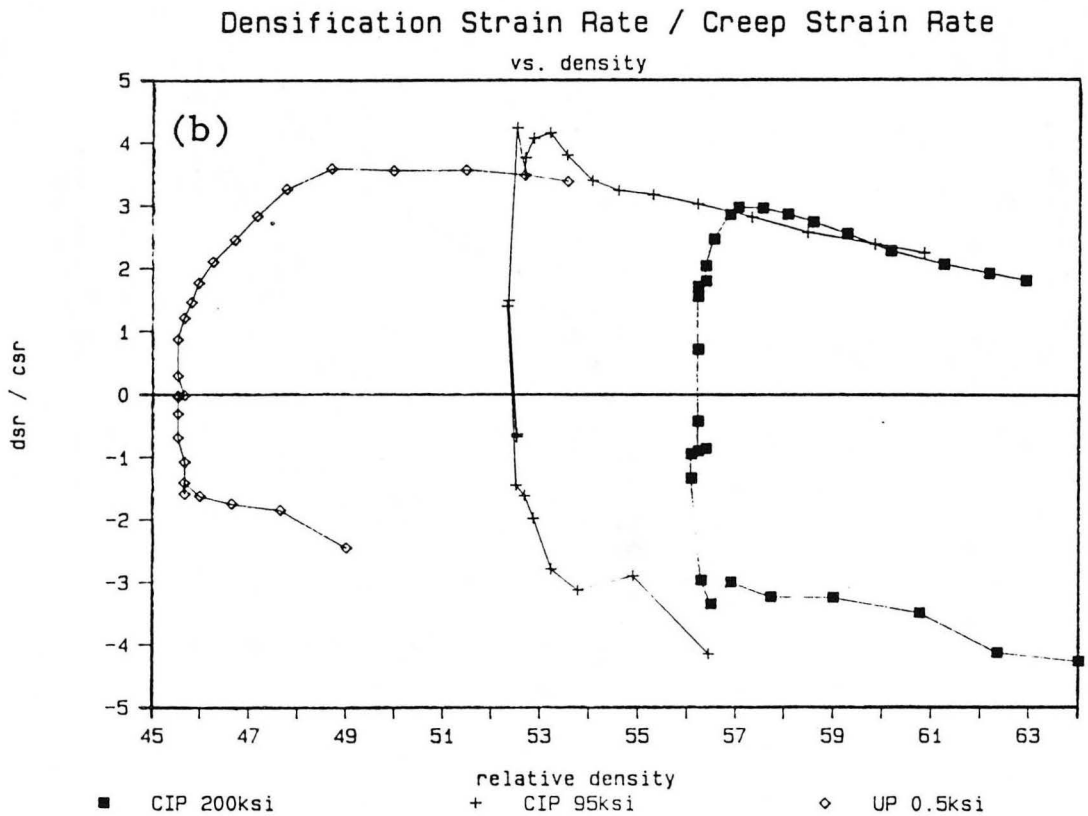
Densification Strain Rate / Creep Strain Rate
vs. density
(b)
dsr / csr
5
4
3
2
1
0
-1
-2
-3
-4
-5
45
47
49
51
53
55
57
59
61
63
relative density
CIP 200ksi
CIP 95ksi
UP 0.5ksi

Figure 20

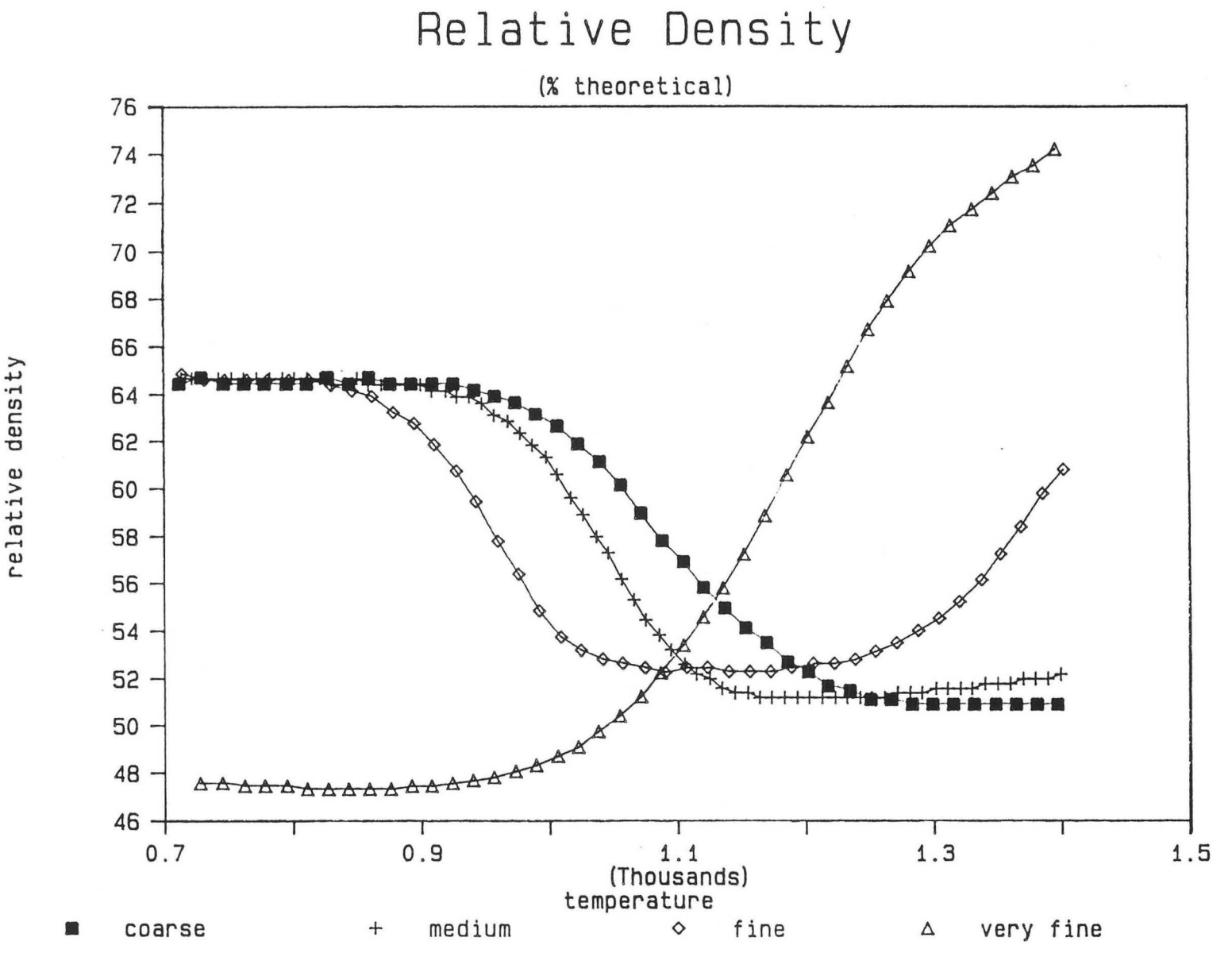
Relative Density
(% theoretical)
relative density
76
74
72
70
68
66
64
62
60
58
56
54
52
50
48
46
0.7
0.9
1.1
1.3
1.5
(Thousands)
temperature
coarse
medium
fine
very fine

Figure 21

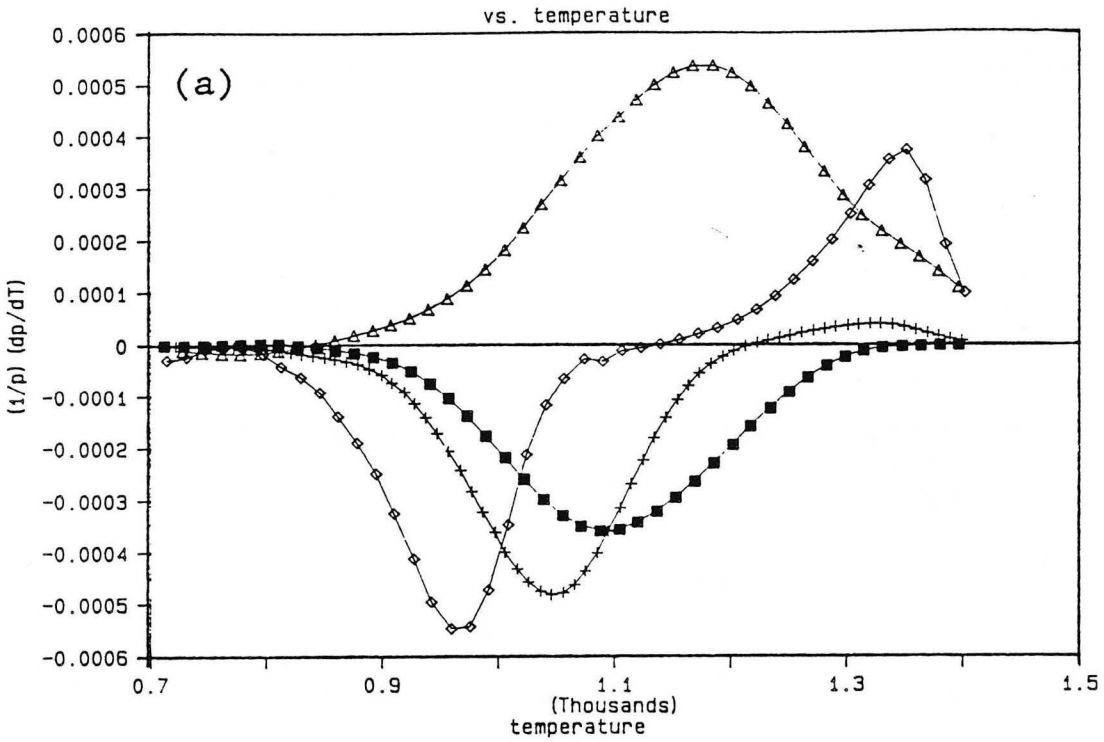
Temperature Derivative of Densification Strain
vs. temperature
(a)
0.0006
0.0005
0.0004
0.0003
0.0002
0.0001
0
-0.0001
-0.0002
-0.0003
-0.0004
-0.0005
-0.0006
(1/p) (dp/dT)
0.7
0.9
1.1
1.3
1.5
(Thousands)
temperature

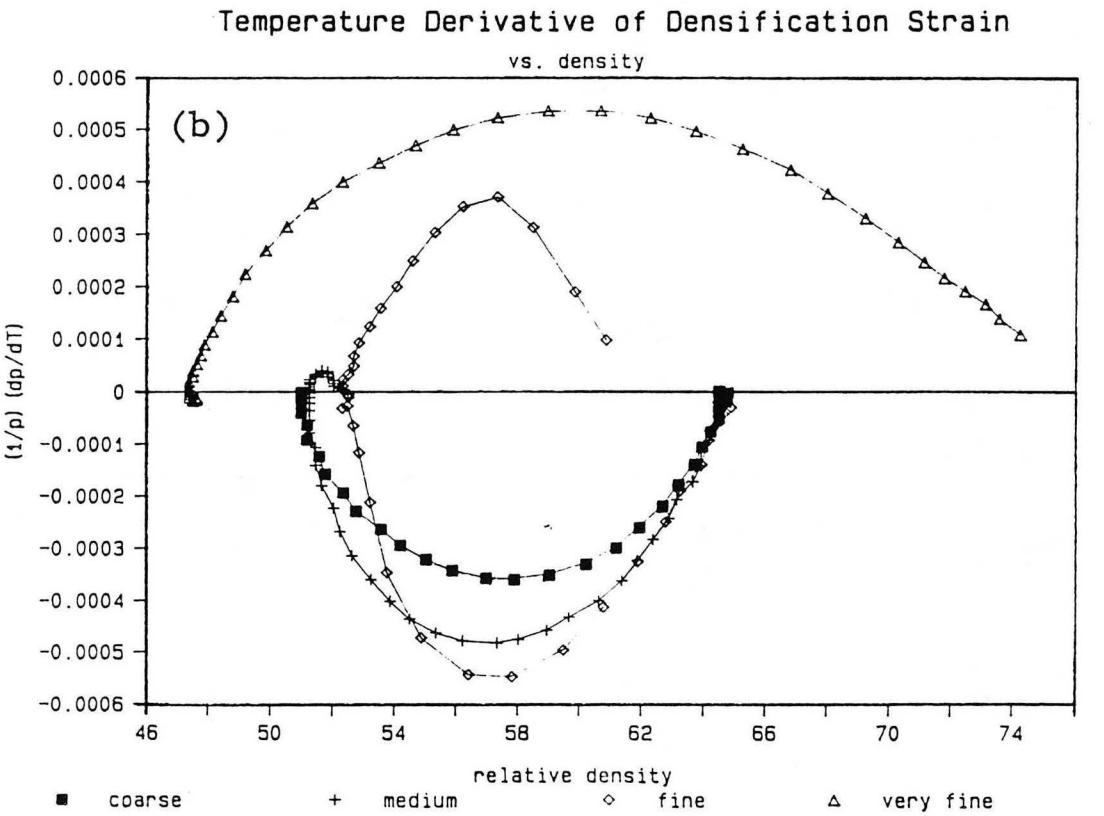
Temperature Derivative of Densification Strain
vs. density
(b)
0.0006
0.0005
0.0004
0.0003
0.0002
0.0001
0
-0.0001
-0.0002
-0.0003
-0.0004
-0.0005
-0.0006
(1/p) (dp/dT)
46
50
54
58
62
66
70
74
relative density
coarse
medium
fine
very fine

Figure 22

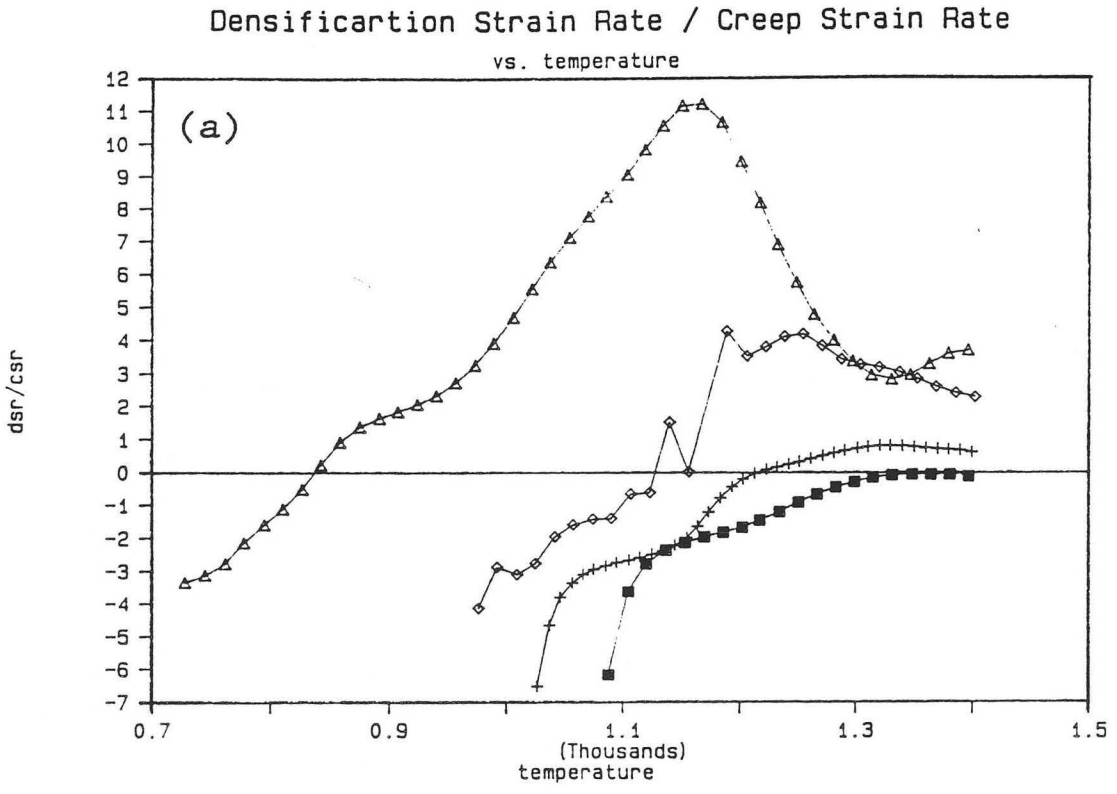
Densificartion Strain Rate / Creep Strain Rate
vs. temperature
(a)
dsr/csr
12
11
10
9
8
7
6
5
4
3
2
1
0
-1
-2
-3
-4
-5
-6
-7
0.7
0.9
1.1
1.3
1.5
(Thousands)
temperature

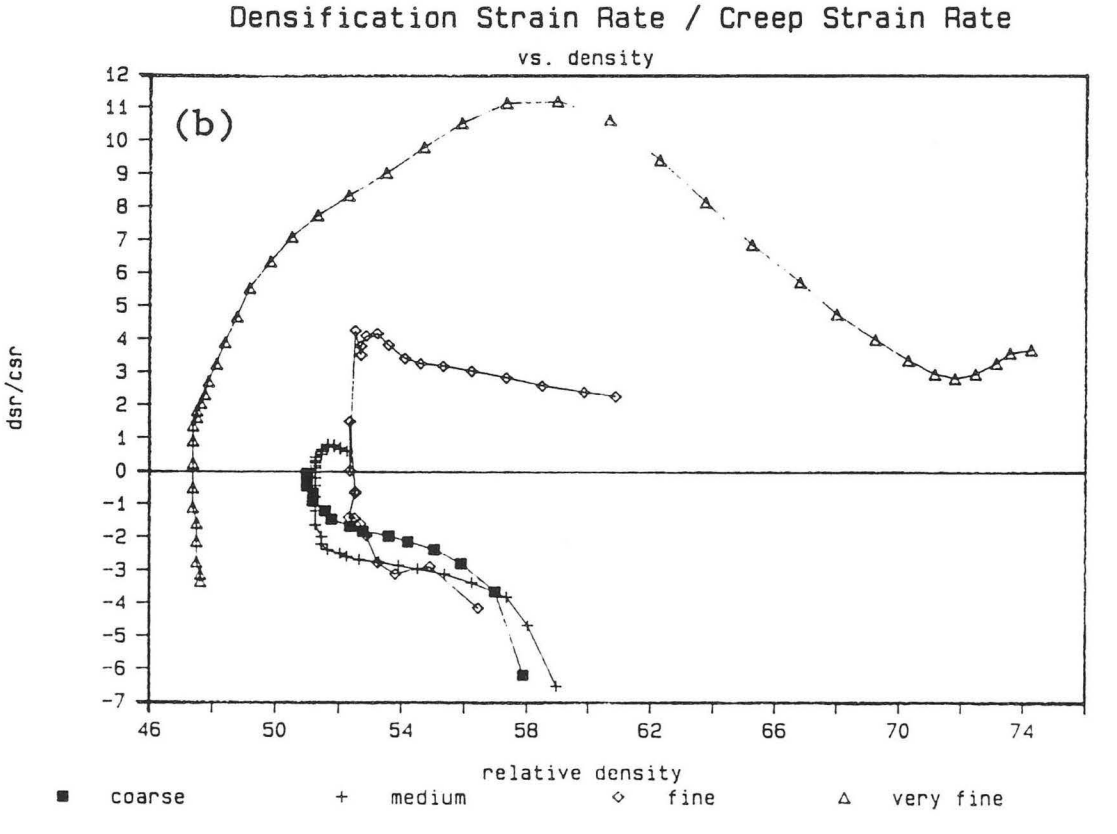
Densification Strain Rate / Creep Strain Rate
vs. density
(b)
dsr/csr
12
11
10
9
8
7
6
5
4
3
2
1
0
-1
-2
-3
-4
-5
-6
-7
46
50
54
58
62
66
70
74
relative density
coarse
medium
fine
very fine

Figure 23

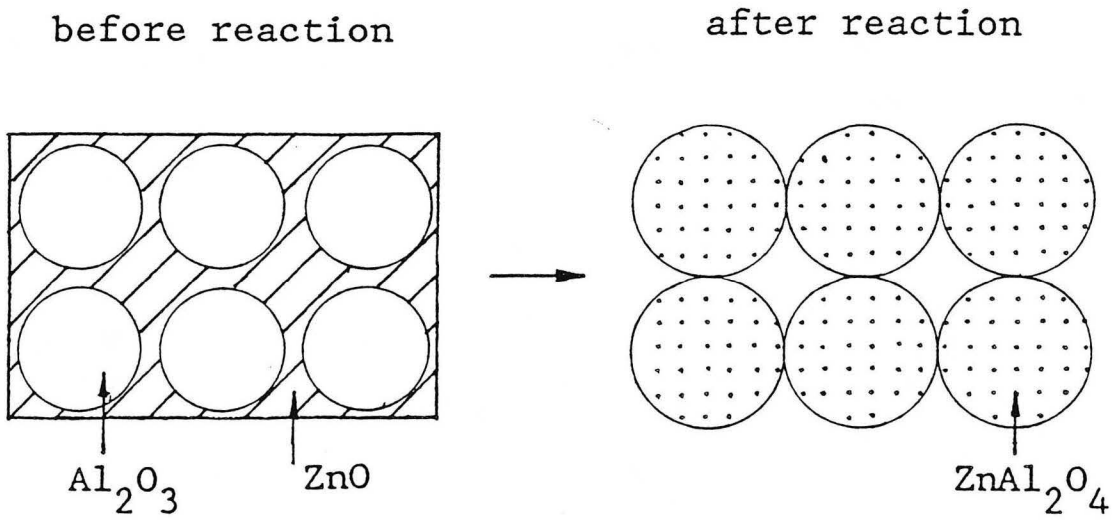

(a)

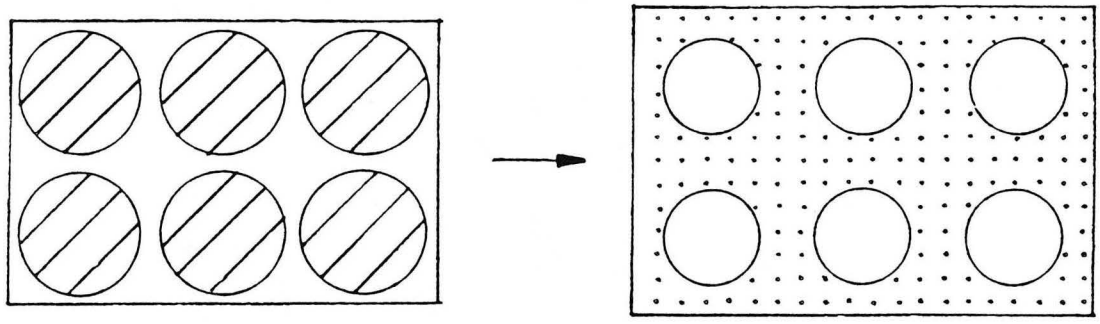

(b)

Figure 24

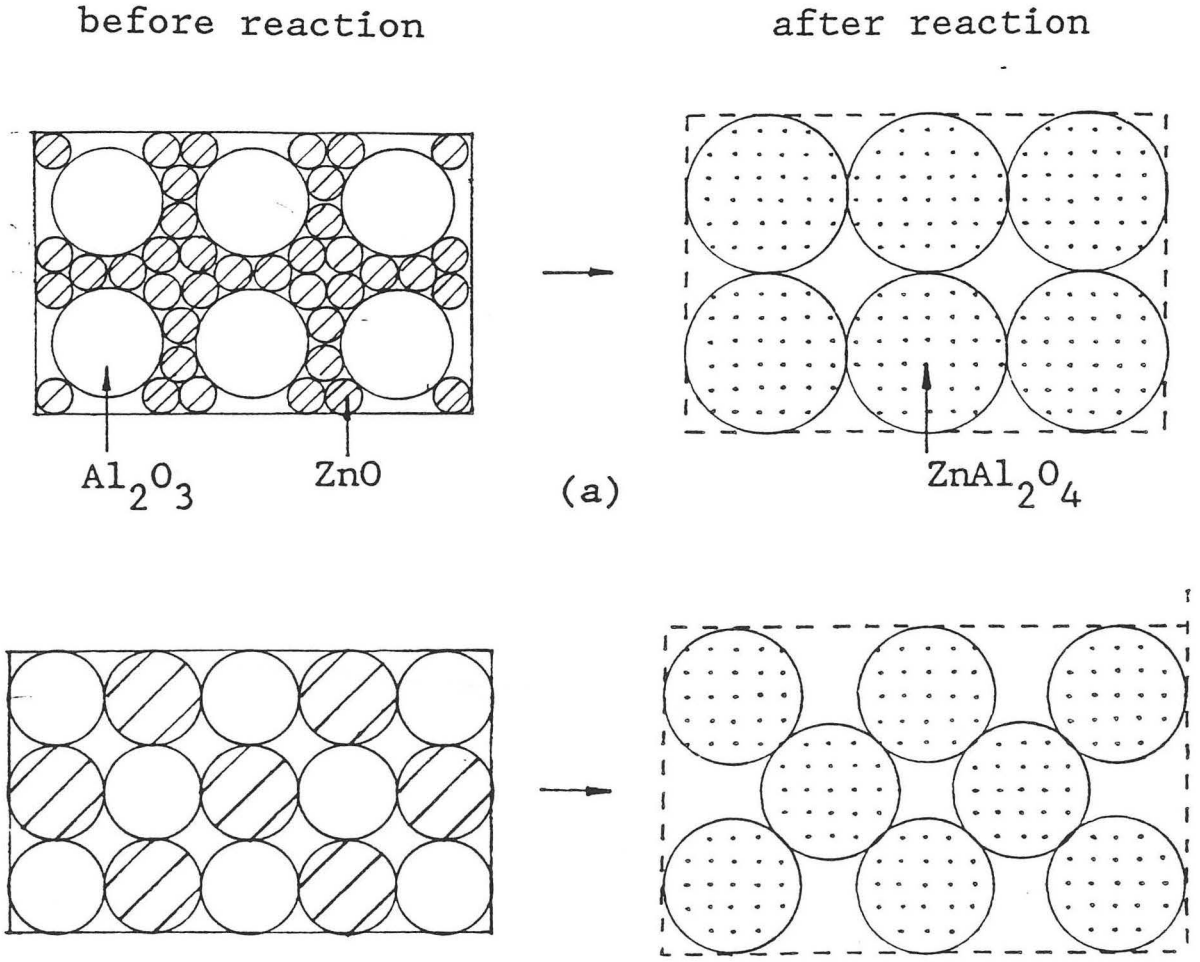

Figure 25

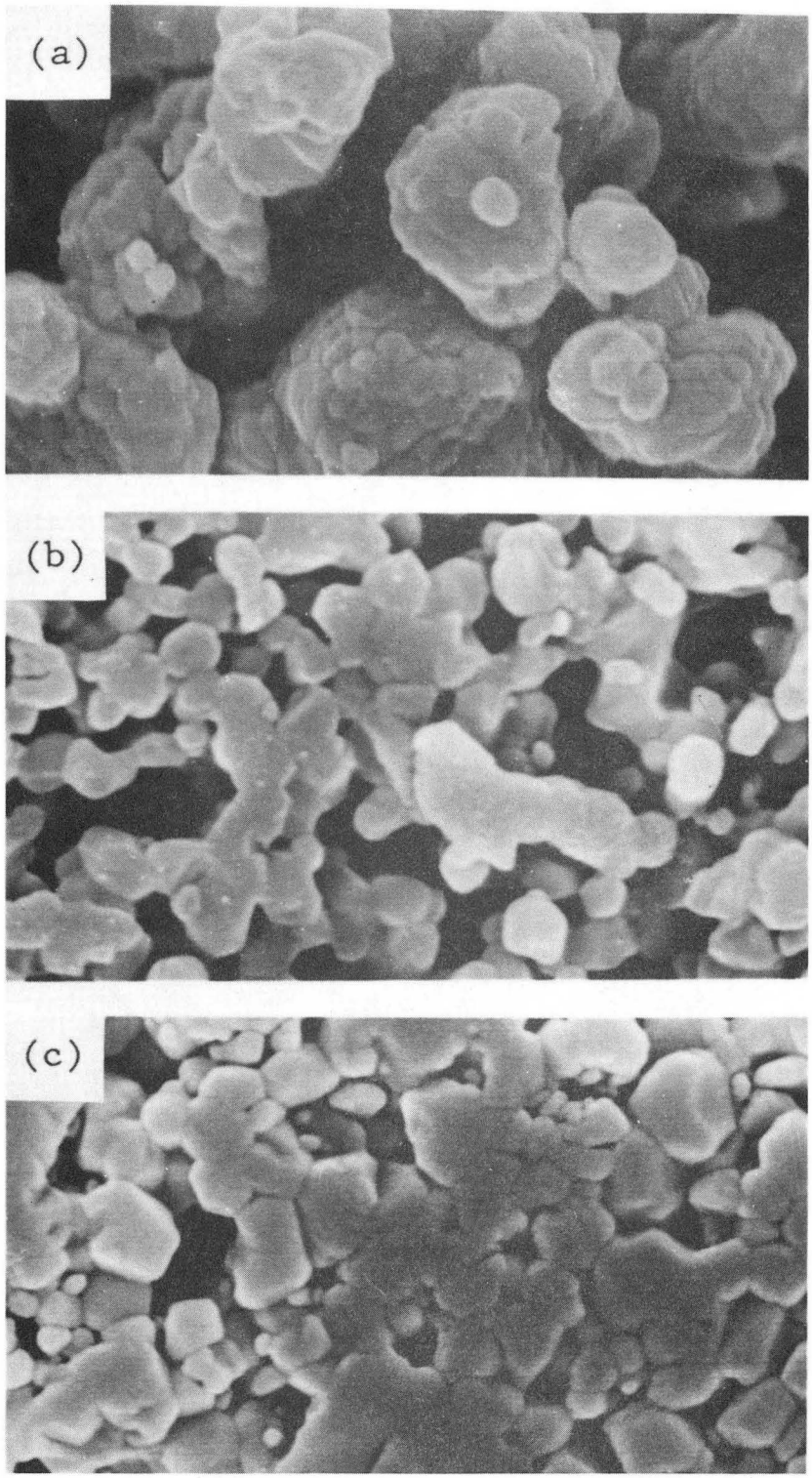

XBB 915-3641

1 μm

Figure 26

LAWRENCE BERKELEY LABORATORY
UNIVERSITY OF CALIFORNIA
INFORMATION RESOURCES DEPARTMENT
BERKELEY, CALIFORNIA 94720